



Classical and Quantum simulations of dislocations in crystals

Author: Santiago Sempere^{*}

Supervised by: Dr. Claudio Cazorla[†]

Co-supervised by: Prof. Jordi Boronat[♣]

University of New South Wales[†] and Universitat Politècnica de Catalunya^{*,♣}

October 17, 2016

Acknowledgements

Above all, I would like to express my most sincere gratitude to my supervisor of the thesis, Dr. Claudio Cazorla. From the very first moment, he tried his best to help me out with all the inconveniences. Aside from guiding and counseling me in all the technical aspects, he effectively transmitted me courage and optimism in those tough times when all you have are non-sense results.

I also want to thank Prof. Jordi Boronat for giving me the opportunity of living this one-in-a-lifetime experience and giving me some advice on everything I needed.

Concerning the technical aspects, I would like to thank the invaluable help offered by Guillem Ferré for providing and helping me with the PIMC code to be able to perform the quantum simulations. Also, thanks to prof. Anna Serra for giving us a beam of light on what was going on with our simulations at the time we were more lost than ever.

Last but not least, I would like to thank my parents for making possible this experience of studying and living in Australia.

Abstract

Dislocations are known to play a key role in the plastic behavior of materials. At the quantum level, experimentalists working on the archetypical bosonic quantum solid ^4He have observed unusual material properties such as *giant plasticity* and *superfluid mass transport*. Although the theoretical explanation for these observations remains elusive, their interpretation has involved the role of dislocations unquestionably. In this thesis, we aim to fulfill the lack of theoretical support for these experiments through atomistic simulations of dislocations. As a first approach, we have characterized the dislocations under classical conditions for a hcp system of Xe with an LJ interatomic potential. Our results reveal the dissociation of the dislocation into two Shockley partial dislocations bounding a broad region of stacking fault. Also, our findings show a very small Peierls Stress τ_p which results in the absence of lattice resistance to dislocation motion at finite temperature. This provides a key insight into a behavior thought to be exclusive to quantum systems. To assess the features of the dislocation at the quantum regime, we employ Path Integral Monte Carlo simulations. We have applied on-the-fly and *a posteriori* methods of analysis to compute the behavior of the dislocation, but none of them have provided conclusive results. Nevertheless, clear evidence for superfluid-like behavior in either the dislocation cores or stacking fault region is not observed in our simulations.

Contents

1	Introduction	4
1.1	A bit of history and motivation	4
1.2	Objectives and outline of the thesis	6
2	Hcp crystals and theory of dislocations	8
2.1	Hexagonal Close-Packed crystals	9
2.2	Crystalline Defects	11
2.2.1	Burgers circuit and Burgers vector	13
2.2.2	Types of dislocations	15
2.2.3	Partial dislocations. Shockley partial dislocations	15
2.2.4	Dislocation motion	16
2.3	Dislocations in hcp structures	18
3	Simulation methods	22
3.1	Classical methods	22
3.1.1	Static simulations	23
3.1.2	Dynamic simulations	24
3.2	Quantum methods	26
3.2.1	Path Integral Monte Carlo (PIMC)	26
3.3	Analysis methods	33
3.3.1	Burgers vector	33
3.3.2	Angular distribution	34
3.3.3	Differential displacement analysis	35
3.3.4	Nearest neighbors analysis	36
3.3.5	Common Neighbor Analysis (CNA)	37
3.3.6	Neighbor-Common Parameter (NCP or CNP) analysis	38
4	Results	40
4.1	Classical regime	40
4.1.1	Zero temperature properties	41
4.1.2	Finite temperature properties	52
4.1.3	About the boundary conditions	56
4.2	Quantum regime	57
5	Conclusions	62
5.1	Classical regime	62
5.1.1	Relaxation	62

5.1.2	Peierls stress	63
5.1.3	Finite temperature	64
5.2	Quantum regime	64
6	Further work	65

Chapter 1

Introduction

1.1 A bit of history and motivation

In the 1970's Alexander Andreev and Ilya Lifshitz at Moscow [1] and Geoffrey Chester at Cornell University [2] suggested the existence of a state of matter in which crystalline order and Bose-Einstein condensation coexist, from their investigations in solid ^4He . They called it *supersolidity* and it was based on the presence of a measurable number of vacancies which at very low temperatures permit a part of a solid to flow on top of the other. This hypothesis aroused big expectations within the experimentalists and some of them started trying to reach this state of matter employing several mass flow and torsional oscillator experiments [3] at temperatures of few dK. The whole idea of the experiment is that if some of the atoms could flow on top of the others, i.e. decouple, this would result in a shift of the oscillation period. First experiments found no evidence of this ability to flow, revealing the non-existence of the so-called supersolidity and killing the enthusiasm of most experimentalists on the topic for over two decades. It was not until Moses Chan and Eusong Kim [4], re-reproducing the experiments previously proposed by Leggett [5], the pioneer in the torsional oscillator, but introducing a higher number of vacancies, observed that there was a change in the period when cooling the solid below 0.15 K. These results were interpreted as a clear evidence of what was likely to be the discovery of a new state of matter, however, remained unclear. From the theory, we know vacancies have a too large formation energy ($\sim 15\text{K}$) so as to be present in a relevant number in the ground state of solid ^4He . Meanwhile, many researchers followed the experiments conducted by Chan and Kim [4]. In 2007, James Day and John Beamish [6] studied the elastic and mechanical properties of solid ^4He , concluding they were originated by the presence of dislocations and their interplay with impurities of ^3He . They found an intriguing coincidence between the temperature at which the shift of period occurred, i.e. 0.15K, with the temperature at which the shear modulus increased sharply. Then, the following question arose: was the change in the period a matter of a change in the structural properties instead of the existence of a new state of matter? This idea gained a major weight afterward, when other experimentalists [7,8] showed a correlation between the moment of inertia and the structure of the solid. Finally, in 2012, a better-designed torsional oscillator was built by Chan and Kim [9] and no more evidence of supersolidity, within the experimental

errors, was found. These new observations made clear that the behavior observed in the first experiments was due to the same causes underlying the mechanical and elastic properties of ^4He observed by Day and Beamish (i.e. dislocations and ^3He impurities).

As a result of the frustrated searches of a new state of matter and following these works, Haziot *et al.* began to study how the stiffness of the quantum solid ^4He was affected by the temperature [10], deriving the conclusions illustrated in Fig. 1.1. They were able to show how the stiffness, i.e. the shear modulus, drops when cooling down the temperature until it reaches a point, $T \simeq 0.15\text{ K}$, where it drastically grows again. This behavior was named as "Giant plasticity". Experimentalists attributed this behavior to the free gliding of dislocations in a particular direction. The fact that below a critical temperature the stiffness grows, what could be counterintuitive, is thought to be due to the pinning of the dislocations by the ^3He impurities, which at such low temperatures are more likely to condensate and mix with the pure solid ^4He . However, this hypothesis lacks either theoretical or experimental evidence to support it.

Recently, Boninsegni *et al.* [11], via atomistic simulations, predicted the existence of superfluidity in the core of a screw dislocation in ^4He , in fact, a 1D Luttinger-liquid system. This prediction led to many following hypotheses involving superfluidity phenomena along dislocation cores, resulting in the prediction of other quantum mechanical properties such as dislocation superclimbing or the syringe effect [12,13]. This work preceded other experiments [14–18] carried out by Ray, Hallock *et al.* showing the existence of "superfluid mass transport". The interpretations of these experiments infer the existence of superfluid dislocation cores, as predicted by Boninsegni *et al.*. However, the very recent work published by Borda *et al.* [19] came to show that the cores were not superfluid, in either the edge or the screw dislocations, invalidating Boninsegni's prediction. Far from a clear conclusion, further tests on this topic are required.

These experiments and theoretical predictions show how very unexpected phenomena can be observed at the quantum crystals and explains why there exists a growing interest in the quantum field from materials' scientists.

From this perspective, we conclude that a theoretical explanation must be done, since many yet-to-be-understood results emerging from the experiments exist and a lack of knowledge in the quantum dislocation field has to be fulfilled. Thus, the aim of our work is to be able to give a proper theoretical explanation of this phenomena by means

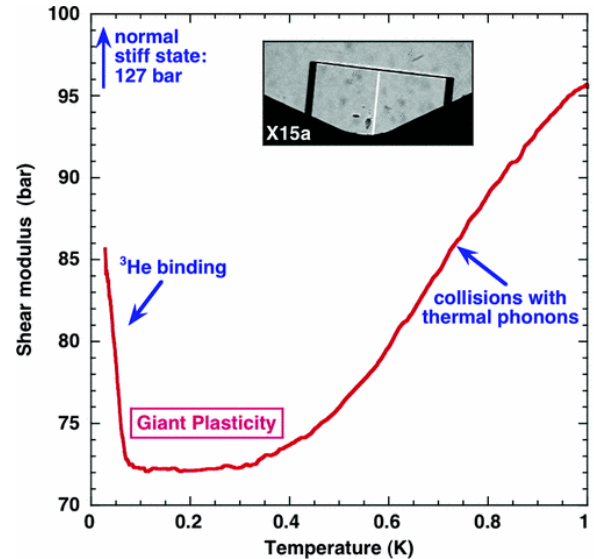


Figure 1.1: Shear modulus of a solid crystal of ^4He . At a temperature of $T \approx 0.2\text{ K}$ the shear modulus is sharply reduced to 72 bar, much less than the normal value of 127 bar. Figure taken from [10]

of atomistic simulations at a quantum level. A first approach from the classical point of view is strictly necessary to set the foundations of the work and to have a reference on what to expect in the quantum regime, although, as we know, everything can happen within it.

1.2 Objectives and outline of the thesis

The primary purpose of this thesis is to give a theoretical explanation of the phenomena observed in the experiments mentioned previously, through the simulation and analysis of atomistic models of ^4He at the quantum regime. In these simulations, we would like to see the existence, or in its defect, the nonexistence, of superfluidity and the appearance of free gliding of dislocations under the application of a minuscule shear stress, what would lead to the so-called giant plasticity. Moreover, an ambitious study of the behavior of the dislocations in the presence of ^3He impurities, to show the role these impurities play in the quantum regime would be liked to carry it out if possible. Several experimentalists claim they have a pinning effect on the dislocations, disabling the free gliding.

In order to accomplish this specific purpose, we have to make a first approach to dislocations from the classical regime to make the path smoother into the quantum dislocations. Furthermore, these first classical simulations could provide us with valuable data to compare with the quantum one. In this sense, we study the properties, both dynamic and static, of an edge dislocation at the classical regime, i.e. using classical potential interactions and at a classical finite temperature.

The outline of the thesis is the following:

1. In chapter 2, we describe from a theoretical point of view the basic players of our game, the hcp crystal and the dislocations. We deeply explain the properties of each of them, doing a brief review in crystallography and showing step by step the features that characterize the dislocations.
2. In chapter 3 we present the different techniques used for the study of the dislocations at the classical and quantum regimes. We mainly introduce the technique of Molecular Dynamics and give rather a simple explanation of how the Feynman's formalism of path integral is implemented into a Monte Carlo method to perform a quantum simulation. Also, we expose the tools used -or tried- to characterize and monitor the dislocation during or after the simulation.
3. Chapter 4 is devoted to showing the results obtained in each of the stages of the project. Consequently, we can distinguish two main parts: the classical regime and the quantum regime. Also, some interconnections and interrelations are done among both methods analyzing differences and similarities between them. By doing this, we can have an idea if whether we can rely on the results obtained at the quantum regime, since not much literature is available, or not. This is the most relevant part of the thesis since we reveal the results of the simulations performed under different conditions. Moreover, we study the relevance of size errors in our system, which can be found to be considerably high and incur wrong

interpretations. This fact enhances the importance of a good classical background, in which we can reach significant systems in our simulations, in order to estimate the effect of the size and bear it in mind for the quantum simulations. In the classical regime, we have used atoms of Xe and a LJ potential, since it is not possible to simulate solid ^4He at such high temperatures without applying very high pressure to give cohesion to the system.

4. In chapter 5, we expose the achieved conclusions from our work and discuss the validity of our experiments due to countless simulation problems, such as system sizes or erroneous interpretations. Also, we will validate some of the hypothesis done by the experimentalists and mentioned in the first chapter in section 1.1.
5. Finally, in chapter 6, we propose a path to follow to improve our work and develop further investigations on this intriguing field, such as the simulation of a crystal of solid ^4He containing dislocations and ^3He impurities.

Chapter 2

Hcp crystals and theory of dislocations

Dislocations are an important kind of defect in crystals, particularly, they are fundamental in materials science since they play a pivotal role in the mechanical property of plasticity. Basic knowledge in crystallography is required to be able to deal with them. Furthermore, we briefly introduce what a crystal is and its basic properties. A crystal is a collection of atoms arranged in a periodic and determined way in the space. Indeed, a crystal can be divided into a finite number of identical replicas that are placed periodically in space. Each of these replicas is called basis and the position they occupy in space and the way they are arranged is called lattice. To sum up, what we have said so far is:

$$crystal = basis + lattice$$

A basis can consist of one or more atoms; in our case and here on it will be composed by a two-atom basis, either formed by Xe in the classical simulations or ^4He for the quantum simulations. On the other hand, the lattice can be one among the 14 lattices postulated by Auguste Bravais, called after him as the Bravais lattices. Due to their periodicity, a Bravais lattice is sufficiently and consistently defined only by their smallest repeated vectors, which constitute the *primitive cell*. All the sites of a lattice can be reproduced by a linear combination of its primitive vectors, this is:

$$R = n_1\mathbf{e}_1 + n_2\mathbf{e}_2 + n_3\mathbf{e}_3 \quad (2.1)$$

However, to simplify it, certain types of Bravais lattices are specified by non-primitive lattice vectors \mathbf{a} , \mathbf{b} and \mathbf{c} . The parallelepiped formed by them is known as *unit cell*. Similarly to the primitive vectors, these lattice vectors can reproduce all the Bravais lattices by the previous analog expression:

$$R = i\mathbf{a} + j\mathbf{b} + k\mathbf{c} \quad (2.2)$$

The use of these vectors is going to be much more common in our study of the dislocations, due to the particular kind of Bravais lattice we face, the *hexagonal close-packed*. In the following section, we will explain thoroughly all the properties and

features of this type of spatial arrangements, and why they are so important and frequently found in nature.

Finally, we introduce the Miller indices. This kind of notation is very convenient and commonly used among researchers since it is a very compact way to show line directions and plane orientations in crystals. For the study of dislocations, the Miller indices will be recurrently used to indicate the dislocation's line direction, its glide plane and the Burgers vector, main aspects of this type of defects, as we will introduce in section 2.2 and see all throughout the work.

Therefore, the Miller indices are used to indicate a line direction or the orientation of a determined plane. A vector \mathbf{l} pointing from one point to another, both in the Bravais lattice, can be expressed as a linear combination of the lattice vectors:

$$\mathbf{l} = i\mathbf{a} + j\mathbf{b} + k\mathbf{c} \quad (2.3)$$

which its corresponding Miller indices are $[ijk]$. By convention, to specify a line direction parallel to \mathbf{l} we use the integers corresponding to the smallest length. To indicate a plane orientation, its normal vector is used and so are the Miller indices. In this case, the Miller indices are defined as (ijk) .

In the next chapter, we will make a slight remark on these points since the hcp structure makes a particular use of the Miller indices that is worth mentioning, the Miller-Bravais indices. This modification is done to simplify the notation for this lattice.

1 H HEX																	2 He HCP
3 Li BCC	4 Be HCP											5 B RHO	6 C HEX	7 N HEX	8 O SC	9 F SC	10 Ne FCC
11 Na BCC	12 Mg HCP											13 Al FCC	14 Si DC	15 P ORTH	16 S ORTH	17 Cl ORTH	18 Ar FCC
19 K BCC	20 Ca FCC	21 Sc HCP	22 Ti HCP	23 V BCC	24 Cr BCC	25 Mn BCC	26 Fe BCC	27 Co HCP	28 Ni FCC	29 Cu FCC	30 Zn HCP	31 Ga ORTH	32 Ge DC	33 As RHO	34 Se HEX	35 Br ORTH	36 Kr FCC
37 Rb BCC	38 Sr FCC	39 Y HCP	40 Zr HCP	41 Nb BCC	42 Mo BCC	43 Tc HCP	44 Ru HCP	45 Rh FCC	46 Pd FCC	47 Ag FCC	48 Cd HCP	49 In TETR	50 Sn TETR	51 Sb RHO	52 Te HEX	53 I ORTH	54 Xe FCC
55 Cs BCC	56 Ba BCC	*	72 Hf HCP	73 Ta BCC	74 W BCC	75 Re HCP	76 Os HCP	77 Ir FCC	78 Pt FCC	79 Au FCC	80 Hg RHO	81 Tl HCP	82 Pb FCC	83 Bi RHO	84 Po SCRHO	85 At [FCC]	86 Rn FCC
87 Fr [BCC]	88 Ra BCC	**	104 Rf [HCP]	105 Db [BCC]	106 Sg [BCC]	107 Bh [HCP]	108 Hs [HCP]	109 Mt [FCC]	110 Ds [BCC]	111 Rg [BCC]	112 Cn [HCP]	113 Uut FI	114 Fl FI	115 Uup LV	116 Lv LV	117 Uus LV	118 Uuo LV
		*	57 La DHCP	58 Ce DHCP	59 Pr DHCP	60 Nd DHCP	61 Pm DHCP	62 Sm RHO	63 Eu BCC	64 Gd HCP	65 Tb HCP	66 Dy HCP	67 Ho HCP	68 Er HCP	69 Tm HCP	70 Yb FCC	71 Lu HCP
		**	89 Ac FCC	90 Th FCC	91 Pa TETR	92 U ORTH	93 Np ORTH	94 Pu MON	95 Am DHCP	96 Cm DHCP	97 Bk DHCP	98 Cf DHCP	99 Es FCC	100 Fm [FCC]	101 Md [FCC]	102 No [FCC]	103 Lr [HCP]

Figure 2.1: Crystal structure of all the elements of the periodic table. Some of them may change their crystal structure under some circumstances of pressure and temperature. In this image are shown the most common found. Notice the importance of the hcp structure, representing almost a 25% of the total

2.1 Hexagonal Close-Packed crystals

The hexagonal crystal family is one of the six crystal families we can find in crystallography. Among all the hexagonal types, it out-stands the close-packed. These type

of arrangements are very common in nature and can be found in many elements, as observed in Fig. 2.1.

Close-packing of equal spheres has represented a recurrent topic of study in history since it has a high importance in what has to do with packing and transportation. The well-known mathematician, Friederich Karl Gauss, demonstrated the biggest fraction of space occupied by spheres, or the highest density, achievable by a lattice is:

$$\rho = \frac{\pi}{3\sqrt{2}} = 0.74048 \quad (2.4)$$

The two close-packed structures that accomplish this statement are the face-centered cubic and the hexagonal close-packed. They mainly differ in the stacking of their vertical planes, although both are created the same way through. The stacking of the hcp is ABAB... whereas the stacking in the fcc is ABCABC... so the third layer, and so on, are different in each case.

It is worth paying some attention to the Miller indices of the hcp structure and how these are conventionally treated since we use a new notation with four indexes called the Miller-Bravais indices.

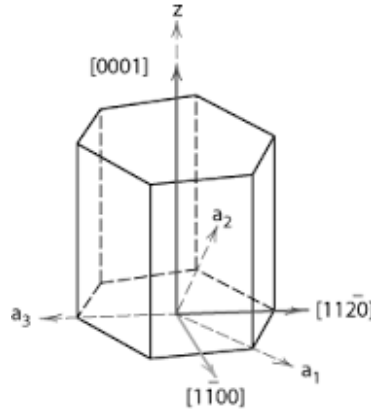


Figure 2.2: Hcp unit cell and the Miller-Bravais indices representation. We can match the x axis with the $[1\bar{2}10]$ direction and the y axis with the $[10\bar{1}0]$

The notation currently used to express line directions and plane orientations is the following:

$$l = i\mathbf{a}_1 + j\mathbf{a}_2 + k\mathbf{a}_3 + m\mathbf{a}_4 \quad (2.5)$$

where a_1, a_2, a_3, a_4 are no more orthogonal vectors. a_1, a_2, a_3 are the vectors describing the basal plane and form 120° with each other, while a_4 is parallel to the z axis. The three components of the base, i.e. i, j and k , must be zero when added together. Therefore, the Miller-Bravais notation to describe a line direction in the hcp lattice would be $[ijkm]$ with the constraint $i + j + k = 0$. The way to define a plane orientation is analogous to the canonic case explained before, and to do so, we refer to the normal vector to the plane and write it as $(ijkm)$. In Fig. 2.2, we provide more details on how to describe this structure.

2.2 Crystalline Defects

All real crystals found in nature show imperfections, either point, line, plane, surface or volume defects. These defects can severely modify the structure and arrangement of the atoms in the crystal and so its properties. By introducing these defects the periodicity of the lattice can be broken, affecting many properties of the crystal such as, for instance, its energy, melting point and density. We can mainly distinguish four types of defects in a crystal. Although this work is predominantly concerned about line defects, called dislocations, let's make a brief introduction to each of them, since they will occasionally appear throughout the thesis.

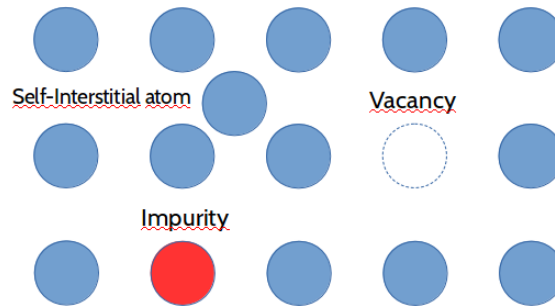


Figure 2.3: Point defects. We can distinguish three principal point defects illustrated in the figure: a vacancy, an impurity and a self interstitial atom.

- Point defects: Three point defects can exist in a perfect crystal, a *vacancy*, a *self-interstitial atom* and *impurities*. The first two types of defects are called *intrinsic* defects since they do not involve another type of atoms than the crystal ones. The first type, the vacancy, consists of removing one atom from its place, so a site in the lattice is empty. The interstitial is formed by placing an atom in between some sites of the perfect lattice. In the illustration Fig. 2.3 we can visualize both types of defects. These type of point defects are very common, for instance, a vacancy represents the key aspect in the theory of semiconductors. Also, we can find what is called *extrinsic defects*, or *impurities*. Impurities also can substantially modify the properties of the crystal. Indeed, we will see in our work how an impurity of ^3He can be crucial when introduced in a crystal of solid ^4He containing a dislocation since their behavior is very conditioned by the presence of each other.
- Planar defect: Better known as *Stacking faults*, this kind of defects can be described as an alteration of the stack in the crystal. In other words, the region where is the defect cannot be built by placing layers of atoms in a regular way anymore. There exist two types of stacking faults: the *intrinsic* and the *extrinsic* stacking faults. These types are widely explained in section 2.2.3. The presence of a stacking fault can play a major role in the plasticity of the material. Once again, this topic will be discussed in more detail in further sections. The presence of a defect and the destruction of the periodicity of the crystals have associated an energy, which is called the *stacking-fault energy*. From the study of the energy surface, one can predict metastable states of low stacking fault energies. For in-

stance, observe Fig. 4.2 in section 4.1.1 where a stacking-fault energy surface is depicted. One can observe the displacements for which there is a minimum in the energy surface γ , that represent the metastable configurations.

- Surface defects
 - Grain boundaries: Crystalline solids are usually formed by a set of *grains* separated by grain boundaries. Each of the grains can contain the defects already mentioned. In the junction of these grains, the atomic arrangement may not be aligned, resulting in a misorientation between the grains. This misorientation causes a very narrow disordered area that can cause a change in the solid crystalline properties.
 - Twin boundaries: When a region of the crystal undergoes a certain homogeneous shear stress that produces a change in the orientation of the crystal, we call it deformation twinning. Fig. 2.4 shows the result of applying a deformation twinning. A very typical case, the illustrated in Fig.2.4, is the one in which the two grains are related by a mirror symmetry. In certain cases, these defects are associated with the presence of a dislocation, then are known as *twinning dislocations*. For instance, see A. Serra *et al.* [20] devoted to the crystallography and core structure of twinning dislocations in hcp metals.

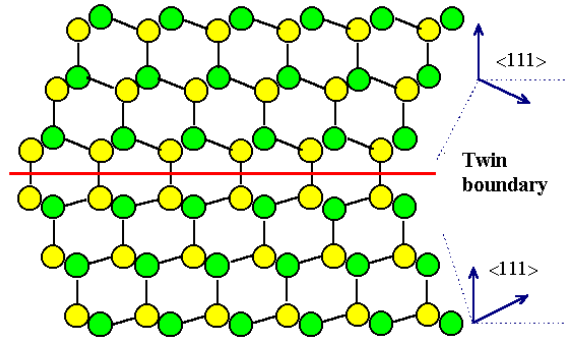


Figure 2.4: Twin boundary defect. The twin boundary shows the plane of the mirror symmetry.

- Volume defects: These defects consist on precipitates, voids and bubbles. They can have a certain importance on the properties of the solid.
- Line defects: **Dislocations**. These type of defects involve rows (or columns) of atoms which are removed or misplaced from the perfect lattice. Even though nowadays there exist several techniques for the direct observation of dislocations in crystals, it was not until the late 1930's when scientists noticed the existence of these dislocations by inference. Strong evidence of this behavior was found when attempting to relate the theoretical and experimental values for the critical shear modulus applied to deform a crystal plastically. In a perfect crystal, the shear stress required to do so, calculated first by Frenkel in 1926, is:

$$\tau_{cr,th} = \frac{Gb}{2\pi a} \quad (2.6)$$

being $\tau_{cr,th}$ the critical applied shear stress to deform the crystal plastically, G the shear modulus, b the spacing between atoms in the same direction as the applied shear stress and a the spacing between atoms in the direction perpendicular to the applied shear stress. Assuming $a \approx b$, from this expression the theoretical critical shear stress results to be at least $\tau_{cr,th} \approx G/10$, which is many orders of magnitude greater than the experimental values of $\tau_{cr,exp} \approx 10^{-4}G$ to $\tau_{cr,exp} \approx 10^{-8}G$. This striking difference between theory and reality manifested the presence of an unknown defect responsible of easing the plastic deformation in a crystal. Later on, when technology developed and it became possible to produce crystals with a very pure structure and almost free of dislocations, the experimental value approached the theoretical one.

Since then, the scientific community has attributed to the dislocation a key role in the mechanical properties of materials, especially in their plasticity. The plasticity is the property of materials that allow them to deform in an irreversible way, contrary to an elastic deformation, where the material returns to its original shape. To give a first flavor on how this mechanism works, as it will be explained afterward, the solid is thought to deform because some of the atomic planes slide over the others.

In conclusion, by the atomistic study of the behavior of a dislocation we are capable of understanding the mechanism of plasticity from a microscopical point of view. We will go back to this topic when we concern the qualitative mechanism of dislocation motion.

2.2.1 Burgers circuit and Burgers vector

Two main features are sufficient to define a dislocation, the *dislocation line* and the *Burgers vector*. Briefly, the dislocation line is the line that runs parallel to the dislocation core and it is commonly indicated by the symbol \perp and represented by the vector ξ .

The Burgers vector is the mathematical tool used to deal with dislocation-like defects in crystals since it offers an unequivocal way to define them and gives a measure of the distortion introduced by the defect. It can be constructed by building a Burgers circuit, which consists of a series of jumps from atom to atom in the crystal describing a closed circuit, in the perfect case, or an opened circuit in the defect case. Hence, the Burgers vector is the vector pointing from the start point of the circuit towards the end point of the circuit. In this manner, if the crystal is perfect, the loop will be completed at the same point where it began; thus the Burgers vector, from here on \mathbf{b} , will be null. On the other hand, if the crystal has a defect, we will have a non-zero Burgers vector which will mean there is a dislocation in the crystal. Several details must be taken into account when doing the Burgers circuit since we have to follow a convention to obtain the same sign for \mathbf{b} . Commonly, the first step is to define a sense, ξ , for the line direction. Then, the flow direction of the circuit is defined with respect to the chosen line accordingly to the right-hand rule. Must be remarked that the jumps between atoms must be a lattice vector, thus in a 2D SC lattice we would have four

possible jumps \mathbf{v} : up $\mathbf{v}_1 = [01]$, down $\mathbf{v}_2 = [0\bar{1}]$, right $\mathbf{v}_3 = [10]$ and left $\mathbf{v}_4 = [\bar{1}0]$. Fig. 2.5 shows how to perform this analysis in a 2D system. The technique can be easily extended to a more complex three-dimensional system.

Furthermore, accordingly to what has been said, the resulting Burgers vector \mathbf{b} is:

$$\mathbf{b} = \mathbf{r}_N - \mathbf{r}_0 = \sum_{i=1}^N \Delta \mathbf{u}_i \quad (2.7)$$

where,

$$\Delta \mathbf{u}_i := \mathbf{r}_i - (\mathbf{r}_{i-1} + \mathbf{v}_i) \quad (2.8)$$

is the difference between where the atom is in the actual, distorted, system and where it should be with respect to the perfect lattice. This value is computed at every step and summed up at the end. This way of computing the Burgers vector will be especially useful when handling with dissociated partial dislocations. Next on, we will explain how we dealt with the issues related to the partial dislocations. Section 3.3.1 is devoted to the implementation of an algorithm to find the Burgers vector and its position.

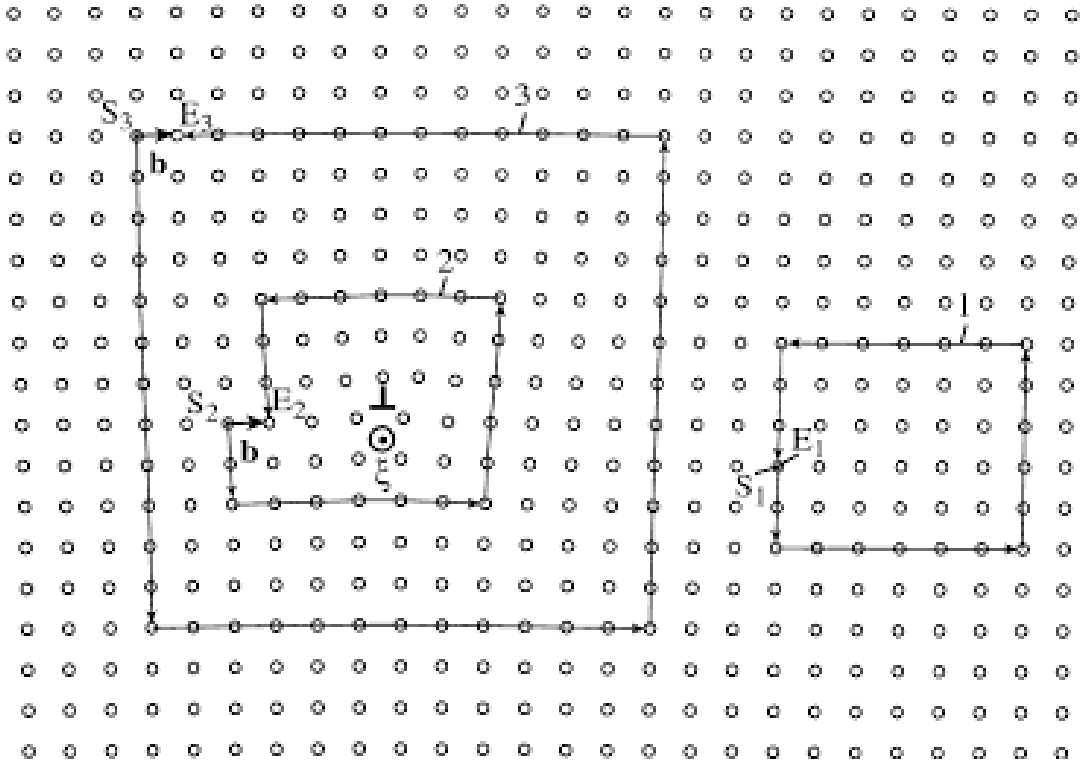


Figure 2.5: Three Burgers circuit depicted in an atomic plane perpendicular to the edge dislocation line in a simple cubic lattice. Notice how circuit 1 and circuit 2 are non-closed since they enclose the dislocation, whereas circuit 3 is a closed loop. E_i and S_i are the corresponding starting and finishing atoms of the corresponding Burgers circuit. The sense of the vector ξ is defined to point out from the paper so that all the circuits flow in the counterclockwise direction. Figure taken from [21]

2.2.2 Types of dislocations

There exist two type of dislocations: screw and edge dislocations. To better understand the geometry and creation of a dislocation let's introduce them through a SC lattice. In Fig. 2.6 we can visualize the concept of both dislocations. Fig. 2.6a is an edge dislocation that has been created by the insertion of a half of a plane in the solid. On the other hand, Fig. 2.6b shows an *screw dislocation* that has been created by 'cut-and-slip' operation. The plane defined by the Burgers vector \mathbf{b} and the dislocation line ξ (section 2.2.1) is called the glide plane. For the edge dislocation, where the Burgers vector is perpendicular to the dislocation line, the glide plane is well-defined, whereas there is not a well-defined glide plane for the screw dislocation because its Burgers vector and dislocation line are parallel to each other.

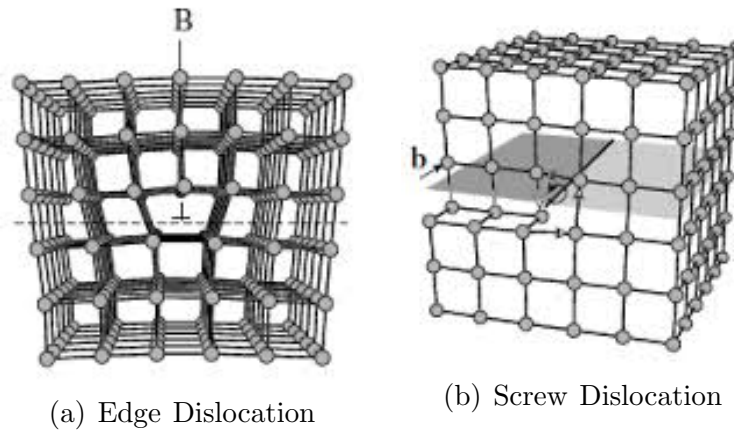


Figure 2.6: Types of dislocations. Figure taken from [21]

2.2.3 Partial dislocations. Shockley partial dislocations

As introduced before, a partial dislocation is a dislocation whose Burgers vector \mathbf{b} has a modulus smaller than a lattice vector, for instance, $\mathbf{b}_p = [\frac{1}{2}0]$. Then, to compute its value, a small correction is made to Eq. (2.6) as follows:

$$\mathbf{b} = \sum_{i=1}^N \Delta \mathbf{u}_i H(\epsilon - |\Delta \mathbf{u}_i|) \quad (2.9)$$

with $H(x)$ being the Heavyside function (Step function). ϵ is a parameter that chooses when the distortion is too big to be accepted in the sum or not, it is calibrated by trial-and-error. Computing the difference between the end and the beginning positions would lead us to an incorrect result, either a whole lattice Burgers vector or a null one. Partial dislocations are found in the presence of a stacking fault. In fact, each of the partial dislocations places at the end of the stacking fault, where the stacking fault merges with the perfect lattice structure. The formation of a low energetic stacking fault in an hcp with a dislocation is very common; therefore, the dislocation tends to split up into two Shockley partial dislocations.

A *Shockley partial dislocation* is a kind of partial dislocation. These are the ones associated with a slip, and its formation can be compared to the one of an edge dislocation in an elastic model. The creation of these partial dislocations is due to a low energetic stacking fault that is more energetically favorable than a single edge dislocation. If we depict the stacking fault energy surface (γ), we would appreciate that the energy of the system after a certain displacement \mathbf{f} shows a minimum, corresponding to a metastable state. In Fig. 4.2 in section 4.1.1 is represented the stacking fault energy surface (γ) for α -Zr and we can observe the minima that explains the dissociation into two Shockley partial dislocations.

2.2.4 Dislocation motion

We can distinguish between two main types of dislocation movement.

- *Glide* or conservative motion: the dislocation moves in the plane formed by the dislocation line and the Burgers vector. This kind of movement is the most typical one and it is even more predominant at low temperatures. This kind of mobility is very anisotropic with respect to the glide plane in the non-screw dislocations.
- *Climb* or nonconservative motion: the dislocation moves out of the glide surface, and, therefore, normal to the Burgers vector. Climbing only occurs at high temperatures when the insertion or emission of atoms is possible. It is called non-conservative motion due to the change in the number of atoms contained in the crystal.

In the screw dislocations the glide plane is not defined; therefore, the only possible movement is gliding.

As mentioned before, the motion of a dislocation is highly related to the mechanical properties of the crystal, in other words, the motion of a dislocation is the mechanism for a crystal to deform plastically. In most cases, to do so we are required by an external force, the driving force, that pushes the dislocation until it moves. This force is applied as a shear stress $\tau = F/A$. The dislocation mobility, which can be expressed as a function of the applied forces on the dislocation $\mathbf{M}(\mathbf{f})$, is mainly influenced by two types of forces: *extrinsic* and *intrinsic* forces. The *extrinsic* forces are those provoked by obstacles or impurities found in the crystal or externally. On the other hand, the *intrinsic* forces are those that arise from the interatomic interactions and due to the lattice resistance. Next section explains the latter type of forces in more detail.

2.2.4.1 Intrinsic resistance to dislocation motion

Within a crystal there exists an energy barrier, when no external forces or energy are added, that oppose the dislocation movement, due to the periodicity of the lattice. In this case, it is called the *Peierls energy barrier*, named after the theoretical physicist Rudolph Peierls, and is the energy needed to break and create the bonds between the atoms in the dislocation core. Hence, this energy depends sensitively on the form of

the force-distance relation between individual atoms, i.e. on the interatomic potential. Fig. 2.7 illustrates the process of breaking and creation of bonds.

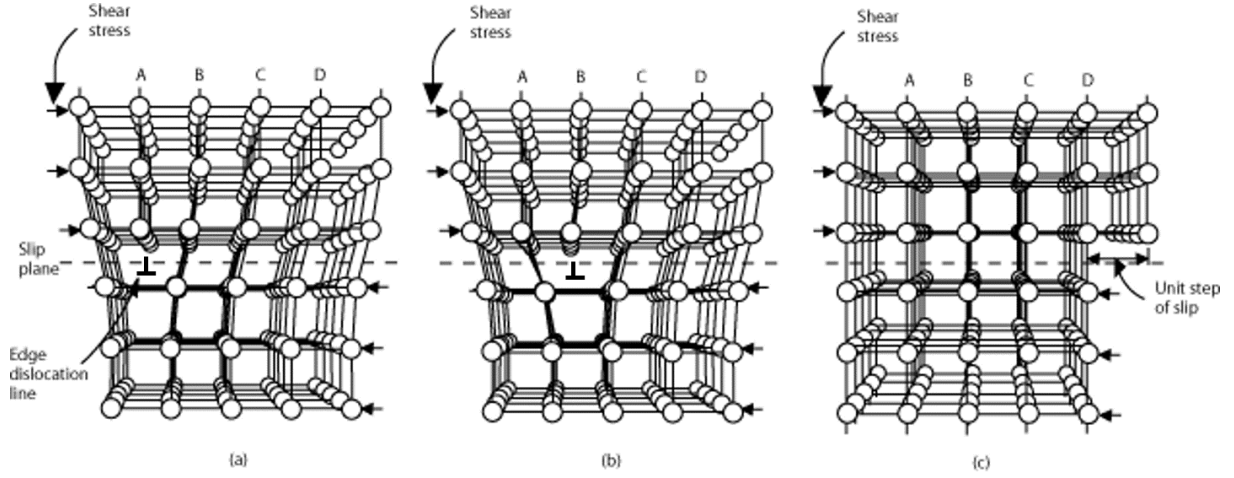


Figure 2.7: Dislocation gliding. A shear stress has been applied and the dislocation moves from left to right, resulting on a plastic deformation in the end. Figure taken from [21].

Another vital concept in dislocation motion is the *Peierls stress*. This is the minimum shear stress required to move the dislocation one lattice vector at $T = 0$. The calculation of this value is essential in all the studies about dislocations since it gives a measure of the lattice resistance of the crystal, which is directly linked to its plasticity. The value of the Peierls stress is related to the *disregistry* of the atoms across the slip plane. In Fig. 2.8 we can appreciate how the atoms are displaced to accommodate the dislocation in the crystal. The disregistry is characterized by the displacement difference $\Delta u = u(B) - u(A)$ between two atoms on adjacent sites above(A) and below(B) the slip plane. The width w of the dislocation is defined as the region where the disregistry is greater than a half of its maximum. In the 1940's Peierls and Nabarro calculated the dislocation energy per unit of length and found it to oscillate with period of $b/2$ and a maximum fluctuation, the Peierls energy, given by [22]

$$E_p = \frac{Gb^2}{\pi(1-\nu)} e^{\frac{-2\pi w}{b}} \quad (2.10)$$

where G is the shear modulus and ν is the Poisson's ratio. The maximum slope of the energy function is the critical shear stress to move the dislocation through the crystal. Dividing by b we get the Peierls stress

$$\tau_p = \frac{2\pi}{b} E_p = \frac{G}{(1-\nu)} e^{\frac{-2\pi w}{b}} \quad (2.11)$$

This simple model agrees much better with the experimental results than Eq. 2.6 , that describes the theoretical shear strength in a crystal. From the expression, notice that the τ_p of a dislocation scales as the negative exponential of the width of the dislocation. Hence, a very wide dislocation core will be very mobile. In general, edge dislocations have smaller Peierls stresses than screw dislocations.

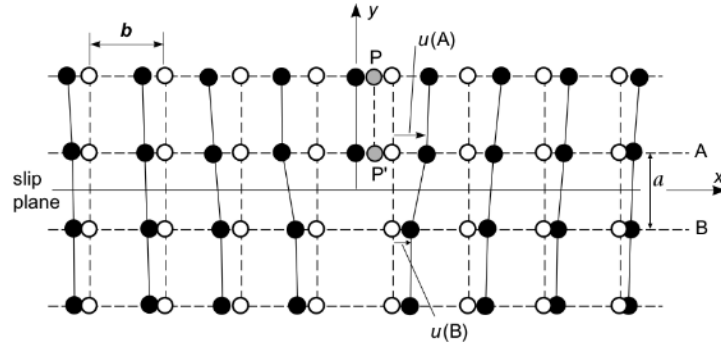


Figure 2.8: Scheme of the registry suffered by the atoms when we introduce the dislocation. The colored atoms indicate the positions after the insertion of the dislocation, whereas the empty circles indicate the positions in the perfect, undistorted configuration. Figure obtained from [22].

2.3 Dislocations in hcp structures

As shortly introduced previously, dislocations in crystals with an hcp lattice structure undergo specific processes that make the dislocation behavior more complex than in other lattices. Making use of the Thompson tetrahedron, Fig. 2.9 for hcp structures (it is normally used for the fcc lattice), we can describe the most important and common dislocations found in hcp structures.

- *Perfect dislocation* with the Burgers vector being one of the vectors in the basal plane. Regarding the tetrahedron this would be either **AB**, **BC**, **CA**, **BA**, **CB** or **AC**.
- *Perfect dislocation* with the Burgers vector perpendicular to the basal plane, represented by **ST** and **TS**. In this case the glide plane is non-basal, is the prism plane ($10\bar{1}0$).
- *Perfect dislocation* with one of twelve Burgers vector of the type **SA/TB**
- *Imperfect basal dislocation* of the Shockley kind, regard 2.2.3, with Burgers vector **A σ** , **B σ** , **C σ** in either one or the other senses.
- *Imperfect dislocations* with the Burgers vector perpendicular to the basal plane, represented by **$\sigma\mathbf{S}$** , **$\sigma\mathbf{T}$** and the counter-sense vectors.
- *Imperfect dislocations* which are a combination of the two latter cases, namely, **AS**, **BS**, etc. Although these vectors go from one atomic site to another one, are still considered imperfect dislocations since their surroundings at each atomic site are not identical and they are not a lattice vector.

The crystallographic representation of these dislocations via the Miller-Bravais indices is found in Table 2.1

Many of the imperfect dislocations are a result of the existence of a low energetic stacking fault. We can distinguish three primary basal- plane stacking faults that do not affect the nearest neighbor arrangements of the perfect stacking ABABAB... , [23]

Two of them are *intrinsic* and called I_1 and I_2 , and the third one is *extrinsic* and called E . The change in the stacking is as follows:

$$ABABABAB... \rightarrow ABABBABA... \rightarrow ABABCBCBCB...(I_1) \quad (2.12)$$

where the middle stage is produced after the removal of a basal layer, what produces a high energy stacking fault. The system goes to the next stage by a slip of $\frac{1}{3}\langle 10\bar{1}0 \rangle$, arriving at a low energy stacking fault.

$$ABABABA... \rightarrow ABABCACA...(I_2) \quad (2.13)$$

Fault I_2 is a result of a slip of $\frac{1}{3}\langle 10\bar{1}0 \rangle$ in a perfect crystal

$$ABABABA... \rightarrow ABABCABAB...(E) \quad (2.14)$$

The extrinsic fault (E) is a consequence of the insertion of an extra plane.

These faults introduce a region in the space where the stacking is different than in the rest of the crystal, thus, in this region a face-centered cubic stacking (ABC) can be found and so have a characteristic stacking-fault energy γ .

The way to explore the stacking-fault energy surface $\gamma(\mathbf{f})$ is to displace a half of a crystal a vector \mathbf{f} while the other half remains in the same position and letting the system go to the equilibrium position. Repeating this procedure all over the space and mapping for $x \in [0, a)$ and $z \in [0, 1.6a)$ we can draw the energy surface. From the data of the energy surface, we can predict and understand why the system goes to one state or the other since it always will try to go to the minima. In chapter 4, where the results are displayed, we will take a look to the stacking energy surface of α -Zr [24] and relate it to the stacking fault and the dissociation of the dislocation observed.

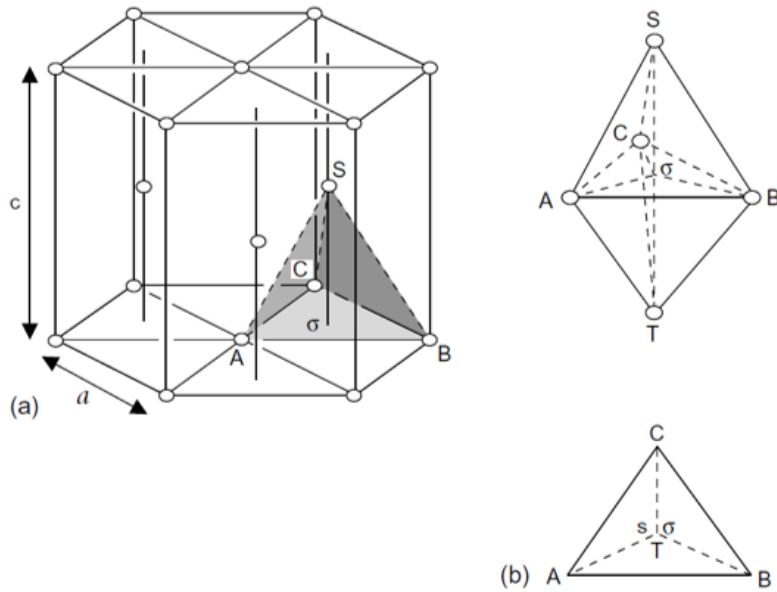


Figure 2.9: Burgers vector in the HCP structure. Taken from [25]

Dissociation of a perfect dislocation into two Shockley partial dislocations

Type	AB	TS	SA/TB	A σ	σ S	AS
b	$\frac{1}{3}\langle 11\bar{2}0 \rangle$	[0001]	$\frac{1}{3}\langle 11\bar{2}3 \rangle$	$\frac{1}{3}\langle \bar{1}100 \rangle$	$\frac{1}{2}[0001]$	$\frac{1}{6}\langle \bar{2}203 \rangle$
<i>b</i>	<i>a</i>	<i>c</i>	$(c^2 + a^2)^{1/2}$	$a/\sqrt{3}$	<i>c</i> /2	$(\frac{a^2}{3} + \frac{c^2}{4})^{1/2}$
<i>b</i> ²	<i>a</i> ²	$c^2 = \frac{8}{3}a^2$	$\frac{11}{3}a^2$	$\frac{1}{3}a^2$	$\frac{2}{3}a^2$	<i>a</i> ²

Table 2.1: Dislocations in Hexagonal Close-Packed lattices

The shortest lattice vector of the HCP is $\frac{1}{3}\langle 11\bar{2}0 \rangle$ and the most common slip planes are (0001) and $\{1\bar{1}00\}$, which correspond to the basal and the first order prism planes, respectively. The preference of the glide plane is determined by the energy and stability of the stacking fault. If the stacking fault I_2 with vector $\frac{1}{3}\langle 11\bar{2}0 \rangle$ exists, then the perfect dislocation AB dissociates into two Shockley partial dislocations bounding a ribbon of stacking fault, which has a fcc-like stacking. The reaction of this process is as follows:

$$\mathbf{AB} \rightarrow \mathbf{A}\sigma + \sigma\mathbf{B} \quad (2.15)$$

which in crystallographic notation is:

$$\frac{1}{3}[11\bar{2}0] \rightarrow \frac{1}{3}[10\bar{1}0] + \frac{1}{3}[01\bar{1}0] \quad (2.16)$$

The geometry of the dissociation is two partial dislocations lying on the basal plane at $\pm 30^\circ$ to the perfect vector (in some texts it refers to the dislocation line, then it would be $\pm 60^\circ$) and the reduction in energy given by b^2 is 1/3, as shown in table 2.1. Notice how after the dissociation the partial dislocations are not a pure edge dislocation anymore, since they have a screw component, although the average screw component for the complete dislocation remains to be null. The method of the Differential displacement introduced afterward in section 3.3 is especially useful to differentiate between the edge and the screw components of the Burgers vector in a dislocation. The schematic representation of this dissociation is illustrated in 2.10

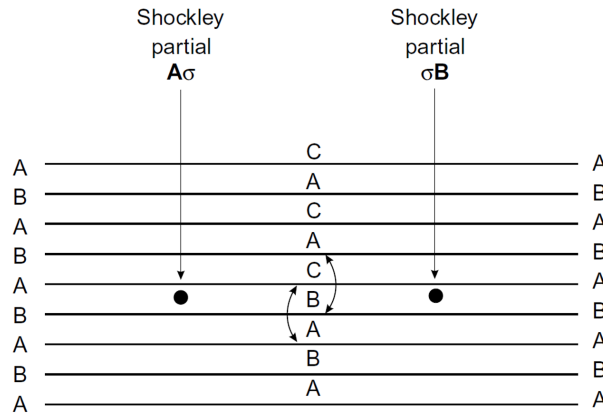


Figure 2.10: Schematic representation of the I_2 stacking fault bounded by two Shockley partial dislocations ($\mathbf{A}\sigma$ and $\sigma\mathbf{B}$). The arrows indicate the two errors in the stacking. Notice how it varies to ABC, corresponding to a face-centered cubic structure. Figure taken from [22].

Despite the existence of other low-energetic stacking faults that led to other dislocation dissociations, we are not going to go into the detail of these, since the principal and most commonly observed one, actually, the only observed in our work, is the previous one.

Chapter 3

Simulation methods

This chapter is devoted to the description of the simulation methods used during the project to understand and simulate the behavior of the dislocations in a crystal under multiple conditions. Firstly, we will introduce the classical methods, in particular, the Molecular Dynamics. It will allow us to analyze the energy and the structural and dynamical properties of the dislocations in classical crystals. We will use this piece of information as a reference set to which compare the results obtained in quantum crystals. Secondly, we introduce the Quantum methods and, especially, the one employed in our simulations, the Path Integral Monte Carlo.

Why do we use atomistic simulations? The interatomic interactions are the fundamental basis underlying the mechanical properties of materials. Therefore, to understand the behavior of dislocations, and, hence, the plastic deformation of a material, it is necessary and sufficient to study the collective behavior of the atoms in a crystal containing a dislocation. Indeed, other researchers have used continuum models, as Pessoa et al. [26], to perform a simulation of the mobility of a dislocation in a quantum crystal. In these cases, the assumption of many classical values for the parameters ruling the model makes the simulation less rigorous and reliable from the physical point of view.

3.1 Classical methods

Quantum mechanical motion and the interaction between the electrons can be important and relevant in the interatomic forces. This fact makes, sometimes, very complicated to describe the interaction among atoms, since a solution of the Schroedinger's equation to describe the electronic interaction is needed to be strictly rigorous. The methods that use this solution are known as first principles methods or *ab initio* methods. The intrinsic difficulty of the Schroedinger's equation makes these methods very costly from the computational point of view, until the point it is unfeasible to simulate a system of more than a few thousands of atoms. Commonly, to describe well the behavior of a dislocation we need much bigger systems that can only be approached by a less sophisticated model. In the following chapters, we explain how this model is.

3.1.1 Static simulations

3.1.1.1 Relaxation

The probability to find a system in an state μ characterized by $\{\mathbf{r}_i, \mathbf{p}_i\}$ in the phase space and in thermal equilibrium at a temperature T is defined by the Boltzmann's law, as follows:

$$p(\mu) = \frac{1}{Z} e^{-\frac{H(\{\mathbf{r}_i, \mathbf{p}_i\})}{k_b T}} \quad (3.1)$$

where

$$H(\{\mathbf{r}_i, \mathbf{p}_i\}) = \sum_{i=1}^N \frac{|\mathbf{p}_i|^2}{2m} + V(\{\mathbf{r}_i\}) \quad (3.2)$$

is the Hamiltonian of the system, Z is the partition function, which ensures the proper normalization of the probability density, defined as:

$$Z = \int \prod_{i=1}^N d\mathbf{r}_i d\mathbf{p}_i e^{-\frac{H(\{\mathbf{r}_i, \mathbf{p}_i\})}{k_b T}} \quad (3.3)$$

and k_b is the Boltzmann's constant. According to this probability distribution, the odds to find the system in a determined state, for instance μ , decreases exponentially with increasing energy $H(\{\mathbf{r}_i, \mathbf{p}_i\})$. Eventually, at the low-temperature limit, the most likely state of the system is at the global minimum of the energy surface $H(\{\mathbf{r}_i, \mathbf{p}_i\})$. The global minimum of the energy, from Eq.3.2, is found when $\mathbf{p}_i = 0, \forall i$. Furthermore, the minimum of the potential energy $V(\{\mathbf{r}_i\})$ gives a good description of the system at low temperatures. Then, a relaxation of a system consists on searching for the minimum of the potential energy $V(\{\mathbf{r}_i\})$ in order to find the most stable state of the system at $T = 0K$.

Searching for minima is a widely studied field, and still an active area of research in computational sciences. There exist several algorithms to seek for the minima of a function, such as the steepest descent algorithm, the Hessian-free truncated Newton algorithm and the conjugate gradient algorithm. In the present work, we have used the Polak-Ribiere version of the more general conjugate gradient relaxation (CGR) algorithm [27].

The CGR algorithm relies on the computation of the atomic forces to displace the atoms in such directions. The algorithm works iteratively until the condition $|\mathbf{F}| < \epsilon$ is reached. It is worth mentioning the CGR algorithm does not guarantee to arrive at a global minimum of the energy, only a local one. Fig. 3.1 illustrates why this can happen. $V(x)$ has three relative minima, two local ones, and the global one. If we use the CGR method for the relaxation, we may end up at a local minimum, since the forces ($F = -\partial V(x)/\partial x$) will be zero. To ensure we arrive at the global minimum, we can use brute-force and run the simulation starting from many randomly selected initial configurations. Clearly, though, it is a very inefficient way to proceed.

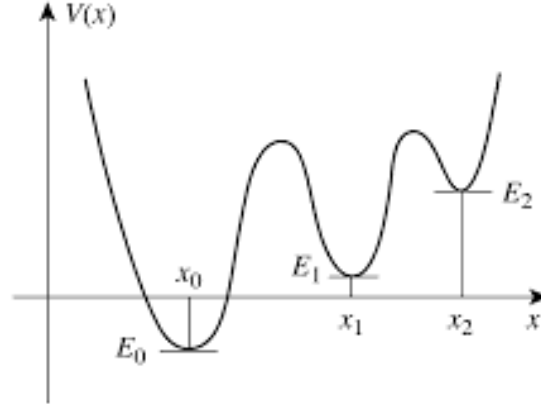


Figure 3.1: An energy function with three local minima E_0 , E_1 and E_2 . The relaxation method can end at either one of the three, not necessarily at the global one E_0 . Figure taken from [21].

3.1.2 Dynamic simulations

3.1.2.1 Molecular Dynamics

Molecular Dynamics constitutes a unique computational method that provides a chance to examine systems from an atomistic point of view [28]. Molecular dynamics is the direct application of the dynamical and mechanical theory developed by Newton and Hamilton. It can be considered as a method of 'particle tracking,' this means we generate the trajectories of the N atoms forming our system. The most relevant factor in this simulations is the pick of the potential and the initial and boundary conditions since the trajectory will come as a result of the numerical integration of the Newton equations. This choice will determine how meaningful the results are. The potential is the way the particles interact, in other words, what forces make to each other and what forces they perceive. Basically, computing a MD simulation means knowing at each time step the positions $\mathbf{r}^{3N}(t) = \{\mathbf{r}_1(t), \dots, \mathbf{r}_N(t)\}$ and the velocities $\dot{\mathbf{r}}^{3N}(t) = \{\dot{\mathbf{r}}_1(t), \dots, \dot{\mathbf{r}}_N(t)\}$ of the set of atoms. The length of the simulation is determined by the timestep Δt and the number of timesteps L , being $T = L\Delta t$ the total simulation time. The typical time scale of the MD simulations is between ps and ns. As said before, to find the trajectories of the particles in a MD simulation we must solve the Newton equations, which are the following:

$$m \frac{d^2 \mathbf{r}_j}{dt^2} = -\nabla_{\mathbf{r}_j} U(\mathbf{r}^{3N}) \quad (3.4)$$

where $U(\mathbf{r}^{3N})$ is a prescribed interatomic interaction potential and $j = 1, \dots, N$. Nevertheless, this equation can not be solved analytically in most cases of interest due to the large number of variables involved. Therefore, we face the need for an integration algorithm to be able to depict the time evolution of the system. Many different types of integrators can be used to solve Eq.3.4; one of the most widely used is the Verlet algorithm, which is formally simple and computationally efficient. This method makes

a basic use of the Taylor expansion and it is computed as follows

$$\mathbf{r}_j(t_0 + \Delta t) = \mathbf{r}_j(t_0 - \Delta t) + 2\mathbf{r}_j(t_0) + \mathbf{a}_j(t_0)(\Delta t)^2 + \mathcal{O}(\Delta t^3) \quad (3.5)$$

where $\mathbf{a}_j(t_0)$ is substituted by the computed forces $\mathbf{F}_j(\mathbf{r}^{3N}(t_0))/m$. Thus, the time evolution is constructed by repeating this calculation at each timestep. The key aspect of Eq.3.5 is the calculation of the forces $\mathbf{F}_j(\mathbf{r}^{3N}(t_0))$, which are computed from the prescribed interatomic potential and determine the movement of the atoms in the system. Other integrators can be more accurate ($\mathcal{O}(\Delta t^5)$), however, they need more computer memory and its implementation can be usually much trickier.

As a summary, an MD simulation consists of the integration of the Newton's equations in discrete time and its efficiency depends on the performance of the force calculations, which must be calculated as simply as possible without compromising the physical description. Hence, the choice of the interatomic potential is a crucial aspect and presents a trade-off between physical fidelity and computational efficiency. Bearing in mind its importance, let's make a deeper regard to the interatomic potential that describes the interaction between particles in an MD simulation. This represents an open-ended topic with a huge amount of literature and still nowadays more and more types of interaction are being developed and implemented.

For the atomic motion, we consider the terms of the one-body, two-bodies,..., N-body interactions

$$U(\mathbf{r}^{3N}) = \sum_{j=1}^N V_1(\mathbf{r}_j) + \sum_{i<j}^N V_2(\mathbf{r}_i, \mathbf{r}_j) + \sum_{i<j<k}^N V_3(\mathbf{r}_i, \mathbf{r}_j, \mathbf{r}_k) + \dots \quad (3.6)$$

The first term is usually neglected except we are in the presence of an external field. The second term is the contribution of two-body interactions and is the most relevant and common term. For many problems this term is sufficient to describe effectively the interaction between the particles.

A widely used interatomic potential in statistical mechanics is the Lennard-Jones potential. It is considered to be a reasonable description of van der Waals interactions between atoms. Also, it can be used for the description of the interaction in some metals [29]. This potential is defined by the following expression

$$V(r) = 4\epsilon \left[\left(\frac{\sigma}{r} \right)^{12} - \left(\frac{\sigma}{r} \right)^6 \right] \quad (3.7)$$

where σ and ϵ are the potential parameters that set scales for energy and separation distances, respectively. Fig. 3.2 shows how this potential makes the particles to repel each other if found to be closer than R_{min} and, otherwise, attract them to the equilibrium value of $r_0 = R_{min}$. This repulsion and attraction interactions are necessary to give *volume* and *cohesion* to the system. If the atoms are not neutral, a Coulombic-type interaction is usually introduced. In some cases, two-body interactions are not enough to describe the system of interest accurately, hence higher-order many-body contributions to the atomic interactions are introduced. This is the case, for instance, of the Embedded-atom model (EAM) [30] that is used in the description of most metals.

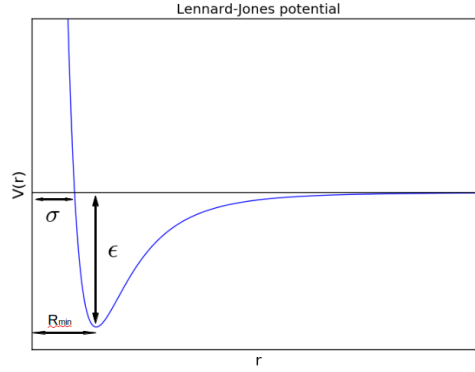


Figure 3.2: The LJ potential $V(r)$. The potential vanishes at σ and has a depth of $-\epsilon$. The absolute force is minimum at $r_0 = 2^{1/6}\sigma$, separations greater or smaller than this value result in attractive or repulsive forces, respectively.

3.2 Quantum methods

We devote this chapter to the Path Integral Monte Carlo method [31, 32] since it is the one used to study the dynamics of the dislocation at very low temperature in this work. Previously to the PIMC algorithm, we introduce the Monte Carlo techniques in general and, in particular, the Metropolis algorithm.

3.2.1 Path Integral Monte Carlo (PIMC)

The Monte Carlo procedures and the Metropolis algorithm

Before making a thorough explanation on how the PIMC algorithm works, let us recall the basics of Monte Carlo methods and how the Metropolis algorithm works. This is an important fact since here lay the roots of the PIMC algorithm.

A Monte Carlo method is a computational way that uses a stochastic sampling to simulate the behavior of a system under certain circumstances. Its applications embrace many different fields, from the computation of an integral to the study of the trends of some financial stocks.

These methods are widely used in condensed matter physics since they enable to study systems characterized by a high number of degrees of freedom and systems in which we are satisfied with a statistical result. In this context, we define a weight w_μ for every possible state of the system μ that defines the probability of the system to be in that state, satisfying $\sum_\mu w_\mu = 1$. Therefore, the expected value for an observable O is given

by:

$$\langle O \rangle = \sum_\mu O_\mu w_\mu \quad (3.8)$$

This sum is computed over all the possible states μ of the system, which in most cases is a huge number. Introducing a method called *importance sampling* allows us to simplify the problem by only choosing the terms of those states in which the system is more likely to be found.

An important Monte Carlo method which is the basis of more complex and used algorithms, in particular, the PIMC, is the so-called **Metropolis algorithm** [33]. This method is based on the theory of the Markov chains and makes use of a probability distribution $p(x)$. The mentioned probability distribution satisfies with the stochastic process we want to perform $\Pi(x|y)$, which is the probability to go from state y to state x , the following expression:

$$\Pi(x|y)p(y) = \Pi(y|x)p(x) \quad (3.9)$$

This only constraint allows us to decompose the stochastic process $\Pi(x|y)$ in two terms:

$$\Pi(x|y) = T(x|y)A(x|y) \quad (3.10)$$

where $T(x|y)$ is again a stochastic process we can sample and $A(x|y)$ indicates the acceptance probability to go from y to x . The choice of T is arbitrary, whereas A is defined from T , satisfying Eq. 3.9. Moreover, T is commonly chosen so $T(x|y) = T(y|x)$, thus

$$A(x|y) = \min(1, \frac{p(x)}{p(y)}) \quad (3.11)$$

This is the main feature of the Metropolis algorithm, and the choice of the probability distribution $p(x)$ will determine the success or the failure of the method. Practically, the implementation of the Metropolis algorithm follows the next procedure, where for simplicity we assume the probability distribution to be the Boltzmann probability distribution $p(x) = \frac{1}{Z}e^{-\beta E(x)}$

- given an state μ , characterized by a variable x_i , we generate a new variable x' from the stochastic process $T(x'|x_i)$, creating a new state μ'
- we evaluate $\Delta E = E(x') - E(x)$, then compute $A(x|x') = \min(1, e^{-\beta \Delta E(x)}) = \alpha \leq 1$
- accept the movement $x \rightarrow x'$ with probability α . Computationally this is done through the generation of a random number r between 0 and 1. Hence, if $r < \alpha$ we accept the movement and $x_{i+1} = x'$, otherwise $x_{i+1} = x_i$, not altering the state of the system.
- perform the same procedure to generate the rest of the variables.

The Metropolis algorithm is a very powerful tool to handle determined systems; nevertheless, it represents two weak points that can not be neglected: the asymptotic correctness of the sampling and the strong correlation between two consecutive variables. The first of the problems can be solved by an equilibration of the system, in other words, discarding the transient regime. The second weakness can be blocked with a technique called *data blocking*. The general idea is to gather M variables in n blocks, with $K = M/n$ variables per block. The average of the estimation of the observable \hat{O} for each block will give a set of values O_j , which if averaged will provide an estimation of $\langle O \rangle$ that is independent of n . Therefore, if K is sufficiently large, the values for O_j can be considered statistically independent and the statistical error can be computed.

Feynman's Path Integral formalism and implementation

The Path Integral Monte Carlo is a simulation method based on the Feynman's Path Integral formalism which has been proven to be very effective for the simulation of quantum systems of condensed bosons, such as solid or liquid ^4He .

The thermal density matrix $\hat{\rho}$ is the key element from which we can obtain the physical properties of the quantum system. This operator is defined as follows:

$$\hat{\rho} = \frac{e^{-\beta\hat{H}}}{Z} = Z^{-1} \sum_i |\alpha_i\rangle e^{-\beta E_i} \langle \alpha_i| \quad (3.12)$$

where \hat{H} is the Hamiltonian operator of the system, being $\beta = \frac{1}{k_B T}$, k_B the Boltzmann constant, and $Z = \text{Tr}(e^{-\beta\hat{H}}) = \sum_i e^{-\beta E_i}$ is the partition function. As shown in the last equation, the thermal density can be also defined in terms of the exact eigenvalues and eigenfunctions of the system, α_i and E_i . Once known the thermal density matrix, the expectation value of a general observable \hat{O} is:

$$\langle \hat{O} \rangle = \text{Tr}(\hat{\rho}\hat{O}) = \sum_i e^{-\beta E_i} \langle \alpha_i | \hat{O} | \alpha_i \rangle \quad (3.13)$$

However, we need to work in the position basis, where the thermal density matrix is written $\rho(R, R'; \beta) = \langle R | \hat{\rho} | R' \rangle$ and, in general, is a function of $6N + 1$ variables, being $\mathbf{R}_i = \{\mathbf{r}_{1,i}, \mathbf{r}_{2,i}, \dots, \mathbf{r}_{N,i}\}$ a set of coordinates. Consequently, in such a basis the equation 3.13 becomes:

$$\langle \hat{O} \rangle = \text{Tr}(\hat{\rho}\hat{O}) = \int d\mathbf{R} \rho(\mathbf{R}, \mathbf{R}; \beta) O(\mathbf{R}) \quad (3.14)$$

The key aspect of the Path Integral formalism is the convolution property of the thermal density matrix. The following equation is the basis of this method:

$$\rho(\beta_1 + \beta_2) = e^{-(\beta_1 + \beta_2)\hat{H}} = e^{-\beta_1\hat{H}} e^{-\beta_2\hat{H}} \quad (3.15)$$

what in position representation is:

$$\langle \mathbf{R}_1 | \rho(\mathbf{R}_1, \mathbf{R}_3, \beta_1 + \beta_2) | \mathbf{R}_3 \rangle = \int d\mathbf{R}_2 \langle \mathbf{R}_1 | \rho(\mathbf{R}_1, \mathbf{R}_2, \beta_1 + \beta_2) | \mathbf{R}_2 \rangle \langle \mathbf{R}_2 | \rho(\mathbf{R}_2, \mathbf{R}_3, \beta_1 + \beta_2) | \mathbf{R}_3 \rangle \quad (3.16)$$

where the identity $\mathbb{I} = \int d\mathbf{R}_2 |\mathbf{R}_2\rangle \langle \mathbf{R}_2|$ is introduced. By repeating these procedure M times we have the following expressions:

$$e^{-\beta\hat{H}} = (e^{-\epsilon\hat{H}})^M \quad (3.17)$$

$$\rho(\mathbf{R}_1, \mathbf{R}_{M+1}; \beta) = \langle \mathbf{R}_1 | \rho(\mathbf{R}_1, \mathbf{R}_{M+1}, \beta) | \mathbf{R}_{M+1} \rangle = \int d\mathbf{R}_2 d\mathbf{R}_3 \dots d\mathbf{R}_M \rho(\mathbf{R}_1, \mathbf{R}_2; \epsilon) \rho(\mathbf{R}_2, \mathbf{R}_3; \epsilon) \dots \rho(\mathbf{R}_M, \mathbf{R}_{M+1}; \epsilon) \quad (3.18)$$

where $\epsilon = \beta/M$ is known as the time step. Then, the succession of points $(\mathbf{R}_1, \dots, \mathbf{R}_{M+1})$ define a "path" in the configuration space. We can notice that the $\hat{\rho}$ operator is formally

equivalent to an evolution operator in imaginary time $t = i\beta$. Eq. 3.18 is exact for any value of $M > 0$ and in the limit $M \rightarrow \infty$, or equivalently $\epsilon \rightarrow 0$, the path becomes continuous.

In order to go further and show an explicit example of this procedure, we make use of the Hamiltonian explicitly, in this case we assume the Hamiltonian for a quantum system made up of N particles of mass m interacting with a pair potential $v(r)$. These kind of Hamiltonians are splitable in two parts $\hat{H} = \hat{T} + \hat{V}$ being

$$\hat{K} = \frac{-\hbar}{2m} \sum_{i=1}^N \nabla_i^2 \quad (3.19)$$

the Kinetic operator and

$$\hat{V} = \sum_{i < j} v(\mathbf{r}_i - \mathbf{r}_j) \quad (3.20)$$

the Potential term

If our purpose is to give an analytical expression, we must determine all the commutators between \hat{K} and \hat{V} . However, from the Baker-Campbell-Hausdorff formula¹, for small imaginary time ϵ we can neglect most terms and $e^{-\epsilon\hat{H}} \approx e^{-\epsilon\hat{K}} e^{-\epsilon\hat{V}}$ with an error of the order of $O(\epsilon^2)$. In fact, the Trotter formula [34]

$$e^{-\beta\hat{K}+\hat{V}} = \lim_{M \rightarrow \infty} [e^{-\frac{\beta}{M}\hat{K}} e^{-\frac{\beta}{M}\hat{V}}]^M \quad (3.21)$$

ensures a good convergence for the process to the exact value of the thermal density matrix. Then we recover an approximation of the thermal density matrix known as *primitive approximation*, which in the positions representation is:

$$\rho_{PA}(\mathbf{R}_1, \mathbf{R}_j, \epsilon) \approx Z^{-1} \int d\mathbf{R}_2 \langle \mathbf{R}_1 | e^{-\epsilon\hat{K}} | \mathbf{R}_2 \rangle \langle \mathbf{R}_2 | e^{-\epsilon\hat{V}} | \mathbf{R}_j \rangle \quad (3.22)$$

The matrix elements $e^{-\epsilon\hat{K}}$ and $e^{-\epsilon\hat{V}}$ can be simply solved in the positions representation. Usually the potential is diagonal in this basis, thus:

$$\langle \mathbf{R}_{j+1} | e^{-\epsilon\hat{V}} | \mathbf{R}_j \rangle = e^{-\epsilon V(\mathbf{R}_j)} \delta(\mathbf{R}_{j+1} - \mathbf{R}_j) \quad (3.23)$$

And the kinetic part becomes diagonal as well if we represent it in the reciprocal space. Therefore, its evaluation is:

$$\langle \mathbf{R}_{j+1} | e^{-\epsilon\hat{K}} | \mathbf{R}_j \rangle = (4\pi\lambda\epsilon)^{-dN/2} e^{-\frac{(\mathbf{R}_{j+1}-\mathbf{R}_j)^2}{4\lambda\epsilon}} \quad (3.24)$$

where d is the dimensionality of the system, $\lambda = \hbar/(2m)$ and we use the definition

$$(\mathbf{R}_{j+1} - \mathbf{R}_j)^2 = \sum_{i=1}^N (\mathbf{r}_{i,j+1} - \mathbf{r}_{i,j})^2.$$

Inserting these expressions (Eqs. 3.23-3.24 in the *primitive approximation* Eq. 3.22) and using it in Eq. 3.18 gives:

$$\rho(\mathbf{R}_1, \mathbf{R}_{M+1}; \beta) = \int d\mathbf{R}_2 d\mathbf{R}_3 \dots d\mathbf{R}_M \frac{1}{(4\pi\lambda\epsilon)^{3NM/2}} e^{-\sum_{m=1}^M [\frac{(\mathbf{R}_{m-1}-\mathbf{R}_m)^2}{4\lambda\epsilon} + \epsilon V(\mathbf{R}_m)]} \quad (3.25)$$

¹ $e^{-\epsilon(\hat{K}+\hat{V})} = e^{-\epsilon\hat{K}} e^{-\epsilon\hat{V}} e^{-\frac{\epsilon^2}{2}[\hat{K},\hat{V}]} e^{-\frac{\epsilon^3}{6}(2[\hat{V}[\hat{K},\hat{V}]+[\hat{K}[\hat{K},\hat{V}]])}$

and, hence, the expectation value is:

$$\langle \hat{O} \rangle = \int d\mathbf{R} \rho(\mathbf{R}, \mathbf{R}; \beta) O(\mathbf{R}) \approx \int \prod_{j=1}^M d\mathbf{R}_j \rho_{PA}(\mathbf{R}_{j+1}, \mathbf{R}_j; \epsilon) O(\mathbf{R}_j) \quad (3.26)$$

applying the boundary condition $\mathbf{R}_{M+1} = \mathbf{R}_M$. The main feature we must notice in this equation is the fact that the product $p(\mathbf{R}_1, \dots, \mathbf{R}_{M+1}) = \prod_{j=1}^M \rho_{PA}(\mathbf{R}_{j+1}, \mathbf{R}_j; \epsilon)$ is positive definite and its integral over the whole space is equal to 1. Therefore, can be interpreted as a probability function and is suitable to work as the probability distribution that rules the sampling of the degrees of freedom in, for instance, the Metropolis algorithm. Thus, many observables that give important physical properties can be computed at any temperature in a rather simple way [31]. Moreover, in virtue of the Trotter formula, as we get closer to the limit $M \rightarrow \infty$ the integral becomes exact and we obtain the exact value of the expectation value \hat{O} . This is the reason why this method is often referred as an *exact method*.

The Classical Isomorphism

The Path Integral Monte Carlo (PIMC) method describes a system of N particles by means of M different configurations \mathbf{R}_M that constitute what we have called the "path" in the imaginary time in the space of configurations. However, this can be interpreted as a classical system made of $N \times M$ particles, each of these called *bead*. Somehow, each of the N initial particles becomes a *polymer* formed by M beads. From the identity

$$\sum_{m=1}^M (\mathbf{R}_{m-1} - \mathbf{R}_m)^2 = \sum_{m=1}^M \sum_{i=1}^N (\mathbf{r}_{i,m-1} - \mathbf{r}_{i,m})^2 = \sum_{i=1}^N \sum_{m=1}^M (\mathbf{r}_{i,m-1} - \mathbf{r}_{i,m})^2 \quad (3.27)$$

we can see the kinetic interaction (Eq. 3.19) of each of the beads and interpret it as if each of the beads is connected to the next one by a spring-like bond. The condition $\mathbf{r}_{M+1} = \mathbf{r}_M$ introduced in Eq. 3.26 guarantees that the first bead is connected to the last bead, forming a closed *polymer*. Now, adding the potential interaction, i.e the interaction between beads of different polymers, does not change this picture. In the primitive approximation, the potential contribution is given by Eq. 3.20 and the interaction between classical beads is identical to the two-body potential of quantum atoms. Nevertheless, these classical polymers interact in a very particular way, since only the beads at the same "time", i.e. imaginary time, in the path interact with each other. This makes the computation so much simpler. Regard Fig.3.3 for a visual understanding of the presented case. In summary, the PIMC method consists of considering the quantum particles as classical ring polymers interacting between them in a particular way. Each polymer consists of a chain of beads connected by ideal springs. This representation enables us to introduce the delocalisation of the particles due to its zero-point motion.

The *action* is defined as minus the logarithm of the density matrix. For a given j , this is:

$$S(\mathbf{R}_{j+1}, \mathbf{R}_j; \epsilon) = -\ln[\rho(\mathbf{R}_{j+1}, \mathbf{R}_j; \epsilon)] \quad (3.28)$$

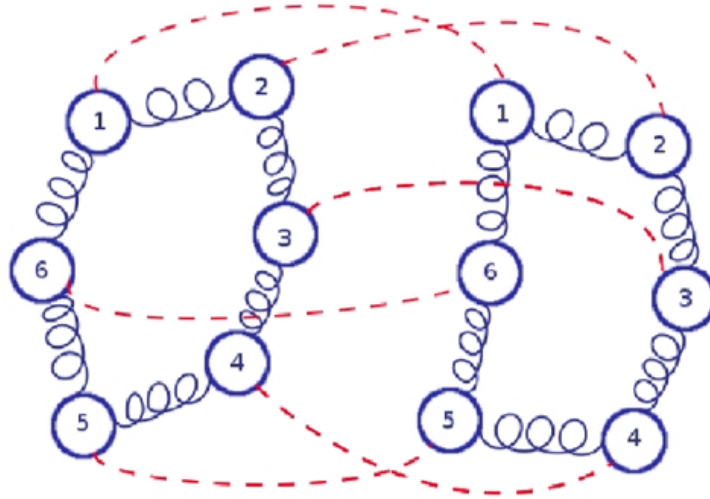


Figure 3.3: Scheme of two classical ring polymers representing the quantum atoms in the PIMC formalism. Each of the numbered circles is a bead and its index is an instant in the imaginary time. The springs connecting each of the beads in each chain shows the kinetic action and the red dashed line represents the potential action acting on beads in the same imaginary time, i.e. same index

so specifies the interaction between the beads in the classical analogy of the quantum system. It strongly depends on the choice of the thermal density, see the review [35] for how to get a "good" action. Particularly, the kinetic action derived from Eq. 3.19 is

$$S_k = \frac{Mk_B T}{4\lambda} ((\mathbf{R}_{j+1} - \mathbf{R}_j)^2) \quad (3.29)$$

Such expression gives an intuitive idea of how the spring-like interaction behaves in the polymers. At high temperatures, the quadratic term is big and, hence, the harmonic potential between beads is strong. Hence, the beads are close to each other and does not allow the polymer to spread in the space, reducing the delocalization of the particle. As the temperature decreases the polymer becomes bigger and the particle is more delocalized in the space, increasing its zero-point motion.

The number of chosen beads M to represent each polymer is essential to get a reliable and well-behaved system and it strongly depends on the temperature. For high T , where no delocalization is found at all, we are able to represent the quantum system by a small number of beads per polymer, being $M=1$ for the classical limit where the polymer shrinks into a single particle. In the other hand, for low temperatures, we need to increase the number of beads M to make a proper representation of the system. Summarizing, the number of beads scales with the inverse of the temperature, i.e. $M \propto 1/T$.

This fact represents one of the weaknesses of this method, since when we approach the most interesting part from the quantum level, this is, at very low temperatures, the computation becomes more and more costly due to the very low efficiency of the sampling of the long chains involved. The way to improve its efficiency is to make a better approximation for the thermal density matrix, in order to work with greater values of ϵ .

The Takahashi-Imada approximation [36,37] and the Chin approximation [38] are among the approximations that make the algorithm more efficient and capable of performing simulations of systems at lower temperatures. We will not get into the detail of these approximations in this work, see each of the mentioned references for a very detailed explanation or [31] for a general overview of these approximations.

The permutation sampling

The previous sections highlight the most important features of the PIMC algorithm, but it is not entirely complete. Indeed, the previous algorithm only holds for systems made up of distinguishable particles. When attempting to deal with quantum many-body systems, we have to take into account the quantum statistics of particles. To recover the right expression for the thermal density matrix ρ , when dealing with the Bose or Fermi statistics, we have to sum over all the possible permutations of the particle labels in one of the two arguments, deriving the following expression:

$$\rho_F^B = \frac{1}{N!} \sum_{\mathcal{P}} (\pm 1)^P \rho(\mathbf{R}_1, \mathcal{P}\mathbf{R}_2; \beta) \quad (3.30)$$

where \mathcal{P} is one of the $N!$ permutations of the particle labels, P is the number of transpositions of the permutation \mathcal{P} and the term (± 1) is either $+$ or $-$ if we are dealing with bosons or fermions, respectively. Analogously to the distinguishable particles case, we can recognize a probability distribution and perform a Monte Carlo procedure to calculate the sum over the permutations. A remarkable detail that changes from the previous sections is the symmetrization of the thermal matrix density, where the boundary condition $\mathbf{R}_{M+1} = \mathbf{R}_1$ becomes $\mathbf{R}_{M+1} = \mathcal{P}\mathbf{R}_1$. $\mathcal{P}\mathbf{R} = \{\mathbf{r}_{p(1)}, \mathbf{r}_{p(2)}, \dots, \mathbf{r}_{p(N)}\}$, $p(i)$ being the label of the particle permuted with the i -th atom. This new condition indicates that the last bead of the i -th polymer is no longer compulsory connected to the first bead of the same chain, but it is connected to the first bead of the $p(i)$ -th polymer. This makes a substantial difference in the mapping onto the classical system, since now exists the possibility that the system is not composed of N identical closed polymers made up of M beads, but it is possible to find out polymers formed by $L \times M$ beads, which represents the permutation cycle between L bosons. To sum up, the explained so far, taking into account the indistinguishability of the particles can lead some of the polymers to open their chains and join other opened polymers to form a longer chain. Concerning the physics of the problem, the formation of longer polymers increases the delocalization of the particles, decreasing the kinetic energy of the particle. If we decrease the temperature enough, the polymers are very spread out and the beads of different polymers are close together making it very plausible that they "collapse" and form a longer chain. In this latter case, we can arrive at a limit for which a macroscopic size polymer is formed and, consequently, a phase transition occurs and we have a fraction of the atoms in a superfluid phase. In a periodic system, the order parameter is measured by the winding number: the number of times a polymer wraps around the periodic boundary conditions.

From a practical point of view, the implementation of these movements are difficult and, thus, makes the computation of the superfluidity unfeasible for systems greater

than $N \sim 100$ atoms. However, the *worm* algorithm, first implemented by Prokof'ev *et al.* and extended to the continuous case by Boninsegni *et al.* (see Ref. [39–41] for further details), provides a tool that allows us to give an efficient description of the thermodynamic properties connected to the bosonic statistics of the quantum systems, such as superfluidity.

3.3 Analysis methods

In this section, we describe the techniques used to estimate the structural and dynamical properties of dislocations in the simulations. Different estimators were tested to determine which one describes more accurately the location and features of the dislocation during the simulation. We performed extensive classical molecular dynamics tests since the computational expense associated with this type of simulations is low in comparison to that of quantum simulations. In view of our MD test outcomes, we decided which estimator was more suitable to be implemented in the PIMC code, both in terms of accuracy and computational affordability.

3.3.1 Burgers vector

As explained in section 2.2.1, the Burgers vector is the property that fully characterizes the dislocation, therefore, it is logic to begin with it in the search of a suitable estimator that allows us to monitor the dislocation.

The implementation of the algorithm to compute the Burgers vector and its position is the following:

1. The first step contains three simultaneous steps
 - (a) Set the dimension of the Burgers circuit. It is important to bear in mind that there is a trade-off in the choice of the dimension of the Burgers circuit since the choice of a large circuit will correspond in a much less costly computation, but the precision in the position of the Burgers vector will be very low. Notice that this method only gives us an intuitive idea of where is the dislocation and it is strongly conditioned by the dimension of the Burger's circuit. In our case, we decided to make a circuit of 2×2 .
 - (b) Choose a determined plane perpendicular to the dislocation line. The Burger's circuit will run over this plane.
 - (c) Choose the initial atom. It is important to recall that we have to explore the whole plane, these means we will have to sample the plane and do many Burgers circuit on it. Fig. 3.4 illustrates the exposed idea.
2. From the initial atom \mathbf{r}_0 move to the nearest atom (\mathbf{r}_i) to the desired position, $\mathbf{r}_i + \mathbf{v}_i$.

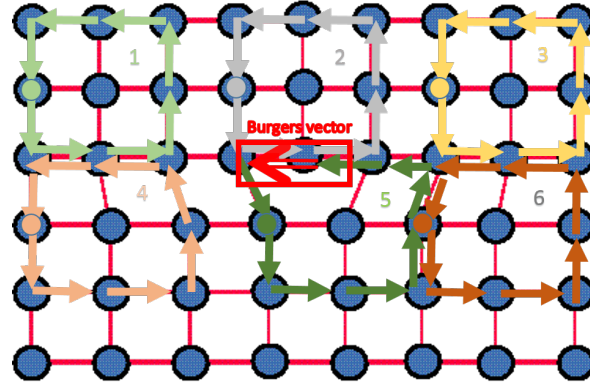


Figure 3.4: Schematic representation of the implementation of the algorithm to compute the position and value of the Burgers vector. We have sampled the chosen plane in 6 different circuits each of them starting from the atom with the big dot in it. The circuit is 2×2 and we observe that the circuit number 5 is not closed, since it encloses the dislocation and we can find the burgers vector.

3. Compute the difference between the actual position of the atom and the place it should have been, as explained in section 2.2.1, $\Delta \mathbf{u}_i = \mathbf{r}_i - (\mathbf{r}_i + \mathbf{v}_i)$
4. Repeat the same procedure for all the circuit, this is for $i = 2, 3, 4$.
5. Compute the Burgers vector from the relative displacements of each step $\Delta \mathbf{u}_i$, as

$$\mathbf{b} = \sum_{i=1}^N \Delta \mathbf{u}_i H(\epsilon - |\Delta \mathbf{u}_i|)$$

6. Repeat the same procedure spanning all over the plane to find the dislocation core

This method of analysis relies on the fundamentals of the dislocation theory, which makes the results very descriptive and complete. The method lacks robustness since it is very sensitive to small fluctuations of the atoms that can lead the algorithm to construct wrong Burgers circuits. Also, the position of the dislocation is not very accurate, since we have a certain range in which the dislocation core must be, delimited by the size of the circuit. Concerning the computational cost, the algorithm computes the nearest neighbors of all the atoms, which is quite costly.

3.3.2 Angular distribution

The introduction of a dislocation in a crystal changes its periodicity and, therefore, there is a structural variation from the perfect crystal. One of the properties that changes is the angular distribution of each atom in comparison with its neighbors. In this context, we have created a parameter per atom that measures the structural variation using the computation of the difference between the angle formed by the atom and its four closest neighbors, considering just one plane perpendicular to the dislocation line, and the angle they would form in the perfect crystal. The parameter is calculated as

follows:

$$\phi_i = \sum_{j=1}^4 (\theta_i^j - \theta_i^{0,j})^2 \quad (3.31)$$

where θ_i^j is each of the four angles formed by the atom and its four neighbors and $\theta_i^{0,j}$ are the angles formed by the atoms in the perfect lattice, i.e. 0° , 90° , 180° , 270° .

The strength of this method lies in the fact of its simple implementation and interpretation; however, it is very sensitive to the atoms fluctuating from their equilibrium positions due to thermal energy. Moreover, it does not provide much information about the dislocation or the stacking fault such as its width or the orientation of the Burgers vector. Once again, the most costly part of the analysis is the computation of the nearest neighbors.

In Fig. 3.5 we can appreciate the result given from this analysis. As observed, the biggest dispersion in the angle is shown in the dislocation cores, allowing us to identify its position. It is a very visual way of localizing the dislocations, however, unfortunately, it does not give us a clear idea about the width of the stacking fault or the Burgers vector.

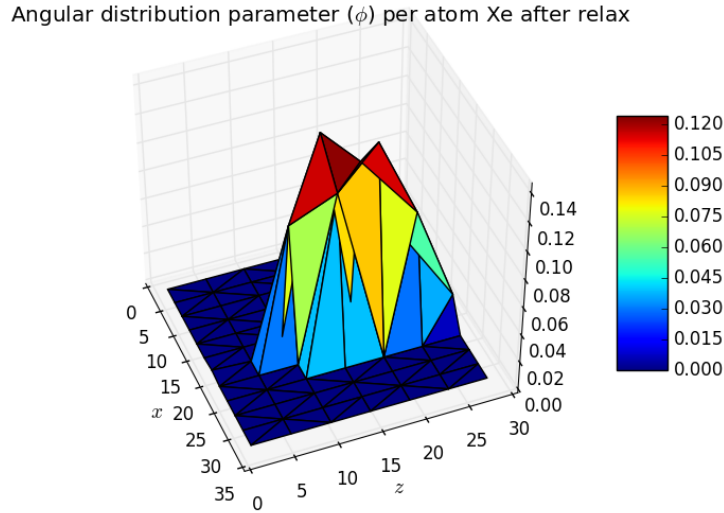


Figure 3.5: Example of the calculation of the angular distribution in a arbitrary y plane of a system containing 2240 atoms ($L_x = 12a$).

3.3.3 Differential displacement analysis

As introduced previously in section 2.2.4, in order to accommodate the dislocation, the atoms across the slip plane are displaced. We can compute the spread of the disregistry associated with a planar edge dislocation by means of the distribution of

the components $[b_x, b_y]$ of the Burgers vector in the glide plane. These components are given by the following expressions:

$$\rho_{b_i} = \frac{d(\Delta u_i)}{dx} \quad (3.32)$$

where $i = x, y$ and Δu_i is described by:

$$\Delta u_i = u_{above,i} - u_{below,i} \quad (3.33)$$

and $u_{above,i}$ and $u_{below,i}$ are defined:

$$u_{above,i} = r_{above,i}^{disloc} - r_{above,i}^{perf} \quad (3.34)$$

where $r_{above,i}^{disloc}$ are the positions of the atoms above the glide plane in the system with the dislocation and $r_{above,i}^{perf}$ are the positions of the atoms in the non-distorted lattice. The definition of the displacement for the atoms below the glide plane is analogous. Therefore, Δu_i is the difference between the displacement of the atoms above the glide plane and the atoms below the glide plane with respect to the perfect lattice positions. The x component of the Burgers vector corresponds to the edge component of the dislocation, whereas the y component refers to the screw component. The total value of the Burger vector can be computed by integrating over all the values of x along the glide plane. This is:

$$b_i = \int_0^{Li} \rho_{b_i} dx \quad (3.35)$$

The computation of the differential displacement gives us much information about the dislocation since from its analysis we can derive, for instance, the presence of a stacking fault ribbon bounded by two partial dislocations, what is the width of the dislocation core and what is the separation between the partial dislocations. In chapter 4, we show many examples of this method of analysis, which has shown up to be extremely useful.

Concerning the computational cost of the method, it does not require the information about the atom-atom distances, which in most cases is the most costly part of the algorithms. For small systems and at finite temperature, it is very imprecise.

3.3.4 Nearest neighbors analysis

An analysis of the nearest neighbors can be very useful to locate the core of the dislocation and, thus, monitor the position of the dislocation during the evolution of the simulation. Basically, we count how many atoms are within a distance r_{cutoff} of each atom. The r_{cutoff} is prescribed to be a value between the distance of the first and second neighbors. A possible cutoff for an hcp system is [42]:

$$r_{cutoff}^{hcp} = \frac{1}{2} \left(1 + \sqrt{\frac{4 + 2x^2}{3}} \right) a \quad (3.36)$$

where $x = (c/a)/1.633$ and a is the lattice parameter.

Therefore, if some of the atoms have a value of nearest neighbors different than 12, which is the coordination number for an hcp lattice, this would mean they are in a region of the crystal where the distortion is high and they can be identified as a part of the dislocation core.

The algorithm calculates the distances between atoms, which is computationally costly. The major strength of this method lies on its simplicity, both of implementation and interpretation. In the other hand, it gives limited information about the features of the dislocation such as, dislocation core width, stacking fault width (although, it is given implicitly) and Burgers vector components.

3.3.5 Common Neighbor Analysis (CNA)

The CNA method was firstly introduced by Honeycutt and Andersen [43] to study the local structure environment. The method consists of creating a diagram for a pair of atoms, α and β , formed by a set of four indexes (1,2,3 and 4). The criterion of the indexes is the following

1. indicates if α and β are nearest neighbors or not. It is 1 if they are and 2 if they are not. Two atoms are nearest neighbors if they are closer than a prescribed r_{cutoff} , which is, in general, the first minimum of the pair distribution function $g(r)$.
2. is the number of common nearest neighbors shared by α and β . In a perfect fcc or hcp lattice is 4.
3. indicates the number of bonds among the common neighbors
4. differentiates between diagrams with same indexes 1, 2 and 3 and different bonding among the neighbors.

Table 3.1 shows the distribution of diagrams in each of the perfect lattices. From this analysis, we can determine the local structure in a crystal and distinguish and recognize the different existing defects.

CNA diagram	fcc	bcc	hcp
1421	1	0	0.5
1422	0	0	0.5
1441	0	3/7	0
1661	0	4/7	0

Table 3.1: Relative presence of each diagram in the fcc, bcc and hcp crystal structures. Table taken from [44]

In our case, this method has shown up to be very useful, so it is a very effective way to localize the dislocations cores and the stacking fault. In section 4.1.1, we show an image where this method of analysis has been used to depict where the stacking fault is since it is a region of fcc structure, and which atoms form the dislocation core. Also, during the simulations at a certain finite temperature, we have used this parameter to monitor the motion of the dislocation.

The salient advantage of utilizing this method is that it is already implemented in the LAMMPS code we employ in the classical simulations. On the other hand, its implementation is not as easy as other estimators, what makes it less suitable to use it for the analysis of the quantum simulations.

3.3.6 Neighbor-Common Parameter (NCP or CNP) analysis

This method of analysis was introduced by Tsuzuki *et al.* [44] and it combines the strengths of two well-known methods, the common neighbor analysis (CNA), presented previously, and the centrosymmetry parameter. The three of them are used to characterize the structure of a crystal and to differentiate structural defects such as dislocations, stacking faults, grain boundaries, cracks and surfaces. However, this new method of analysis was chosen as the most appropriate for our case since, on one hand, the CNA has a complex way of implementation and it may be intricate to interpret, and, on the other hand, the CSP is only fully defined for centrosymmetric crystals, i.e. fcc and bcc. Although this does not prevent us from using them, we would incur a loss of accuracy compared to the CNP. Also, another advantage of this method over the CNA is that it does not require an explicit knowledge about what are the opposite neighbors, what for the hcp structure can be a tedious and a not well-behaved numerical task.

The CNP consists on the computation of a single parameter Q_i per atom. Depending on the value given by this parameter, that atom will be arranged in a determined structure. The definition of Q_i follows:

$$Q_i = \frac{1}{n_i} \sum_{i=1}^{n_i} \left| \sum_{k=1}^{n_{ij}} \mathbf{R}_{ik} + \mathbf{R}_{jk} \right|^2 \quad (3.37)$$

where the index j sums over the n_i nearest neighbors of atom i and index k goes over the n_{ij} common neighbors between atom i and its nearest neighbor j . \mathbf{R}_{ik} is the vector pointing from atom i to atom k . Respectively, \mathbf{R}_{jk} is the vector pointing from atom j to atom k . For the bcc and fcc lattices this parameter is null and for the hcp lattice, its value depends on the lattice parameter. In the Path-Integral Monte Carlo algorithm, we must make use of the beads formalism to compute this parameter, thus the definition of the parameter Q_i results to be:

$$Q_{i,j} = \frac{1}{n_i} \sum_{i=1}^{n_i} \left| \sum_{k=1}^{n_{il}} (\mathbf{r}_{k,j} - \mathbf{r}_{i,j}) + (\mathbf{r}_{k,j} - \mathbf{r}_{l,j}) \right|^2 \quad (3.38)$$

where $Q_{i,j}$ is the NCP parameter for the bead j of atom i . The vector $(\mathbf{r}_{k,j} - \mathbf{r}_{i,j})$ is analogous to the vector \mathbf{R}_{ik} of the classical expression and indicates the vector pointing from bead j of atom k to the bead j of atom i . Now, to obtain the NCP parameter per atom we have to sum over all the beads of each atom,

$$Q_i = \frac{1}{n_b} \sum_{j=1}^{n_b} Q_{i,j} \quad (3.39)$$

This would give us the value of the parameter Q_i that allows us to identify the local lattice structure within a crystal.

The main strengths of this method are its simpleness of implementation and interpretation. Computationally, it is costly since it requires the computation of the atom-atom distances.

Chapter 4

Results

This chapter is devoted to the presentation of the results obtained from our simulations. It is divided into two major parts: the results of the simulations within the classical regime and the ones for the quantum regime. In each of them, we will mention the path we have followed to achieve the ultimate goal if achieved.

4.1 Classical regime

Before going into the detail, we make an overview of what we have done in this part, how we have done it, what we expected and what we have actually obtained. This is important to understand why we have proceeded as we did since many unexpected issues have appeared during the simulations.

The aim of the simulations under classical conditions was to make an approach into how dislocations behaved and to create an estimator that allowed us to characterize and monitor the dislocation during the quantum simulation. The pursuit of a robust, accurate and fully descriptive estimator is one of the key aspects of this work. Although some MD codes as LAMMPS do include a package for treating with dislocations, we had the need to create our own one that enabled us to implement it in the PIMC code.

We have used an already built code to perform the MD simulations. This is the Large-scale Atomic/Molecular Massively Parallel Simulator, mostly known as *LAMMPS* [45]. The use of an already developed code to perform a simulation has its weaknesses and strengths. The strengths being obvious, a significant weakness is the fact that is much harder to understand and solve a problem occurring in the simulation since one has no access to the code and is trickier to follow the path to the source of the problem.

In the classical simulations, we have used a system formed by Xe atoms arranged in a hexagonal close-packed configuration interacting through a Lennard-Jones interatomic potential. The motive why a system of Xe is considered instead of ^4He , which was our objective, is that under classical conditions ^4He is not a solid unless a huge pressure is applied. The application of a high pressure could lead the simulation to unexpected behavior; therefore, we rather use Xe, which is also a rare gas and its melting point $T_m = 161,4K$ makes it a solid for a broad range of temperatures under pressure-free

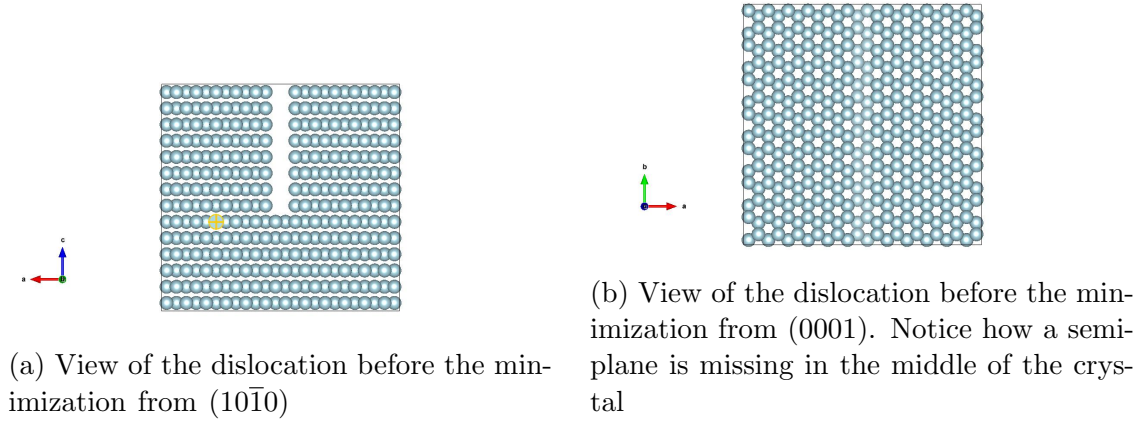


Figure 4.1: Illustration of the way the dislocation has been introduced into the crystal and the resulting system. We have used VESTA [46] to visualize the atomic structures.

conditions.

As introduced in section 3.1, the choice of the potential is a key aspect in the classical simulations. In the present work, we use a Lennard-Jones (6-12) potential with $\epsilon = 1.77 \text{ kJ/mol}$ and $\sigma = 4.10 \text{ \AA}$ which makes an efficient representation of the interaction of atoms in a crystal of Xe. In some cases, this potential is shifted to be zero for a determined r_{cutoff} to avoid discontinuities in the energy due to the jump at the cutoff. This alteration of the potential may affect the energy, but it does not influence the forces on the atoms or their trajectories. We shift it to avoid the CGR stopping due to a discontinuity in the energy.

Introduction of the dislocation into the system

The procedure to introduce the dislocation into the system is very simple, we just remove one semi-plane of a perfect lattice, getting the system shown in Fig. 4.1

This could seem a very careless way of introducing the dislocation, but we proved that the system resulting after the minimization of the potential energy and the box dimensions is analogous to the one obtained by inserting the dislocation in a more formal way, such as Osetsky and Bacon suggest in [47]. They propose to create two perfect crystals, one with N layers and the other with $(N - 1)$ and strain them to have the same area to be able to join them into one single crystal with a dislocation.

4.1.1 Zero temperature properties

In this section, we consider the part of the simulations where the minimization of the potential energy and forces is performed. This section contains two differentiated parts, firstly we treat the minimization itself and we analyze the resulting state and, secondly, we perform the analysis of a crucial feature in dislocation theory, the Peierls stress. In the second part, we present the techniques used to compute this property, since one of them substantially differs from what the literature commonly suggests.

4.1.1.1 Relaxation

The minimization of the potential energy for the system, also referred as relaxation, is done via conjugate gradients method until the energy can not be reduced anymore and the forces are lower than $|\mathbf{F}_{ij}| < 10^{-10} \text{eV}/\text{\AA}$. We concluded that the most consistent way to relax the system was considering a fully periodic system with PBC in all three axes. All the boxes used for the performance of the simulations in this section have a lattice parameter $a \approx 4.26 \text{\AA}$ (it might change due to the enlargement of the box during the box relaxation to minimize the stresses). The value of the Burgers vector is a whole lattice vector, so $\mathbf{b} = (a, 0, 0)$.

A key aspect in the dissociation of the dislocation is the presence of a metastable stacking fault. This state is found where there is a minimum in the stacking fault energy γ . The study of the stacking fault energy surface can give a hint on what to expect and how the stacking is going to change. In the present work, the γ has not been depicted due to a lack of time, but a similar energy surface to the one that would have been obtained can be seen in Fig. 4.2, taken from the work published by Khater and Bacon [24]. There is a metastable fault that indicates the kind of dissociation that will lead the system when we introduce the dislocation.

We use the mentioned system and minimize its potential energy employing a conjugate gradient algorithm. We also allow the box to relax, so we reduce the forces and stresses as much as possible. At this point, we analyze the resulting configuration to determine whether there is still a dislocation or it has dissociated into two partial dislocations, or if it has already moved during the minimization or not. To do so, we use the estimators we have developed previously, and the results obtained are the following. The system has reached the configuration shown in Fig. 4.3 where the atoms colored in blue are the ones belonging to the stacking fault (fcc stacking), the ones colored in red belong to the dislocation core and the pastel colored are the ones belonging to the nondistorted hcp lattice. To perform this differentiation, we have used the CNA parameter to distinguish between the different arrangements that are found in the crystal.

Moreover, it is very informative the computation of the differential displacement of the atoms in the glide plane to assess the disregistry of the atoms and depict where

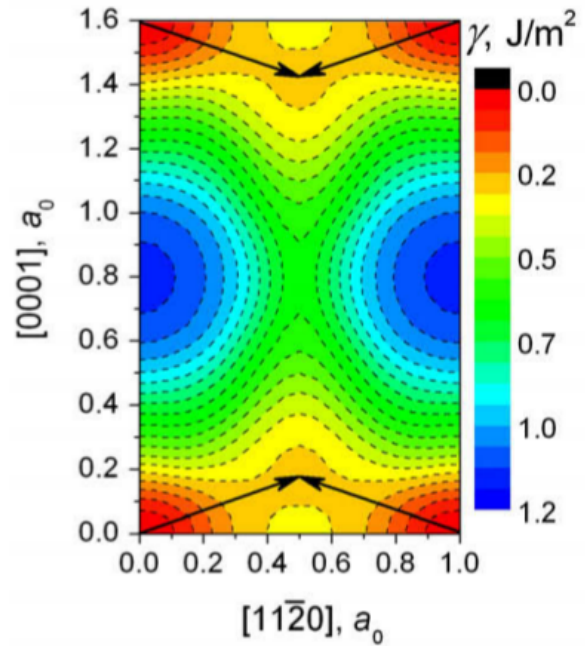
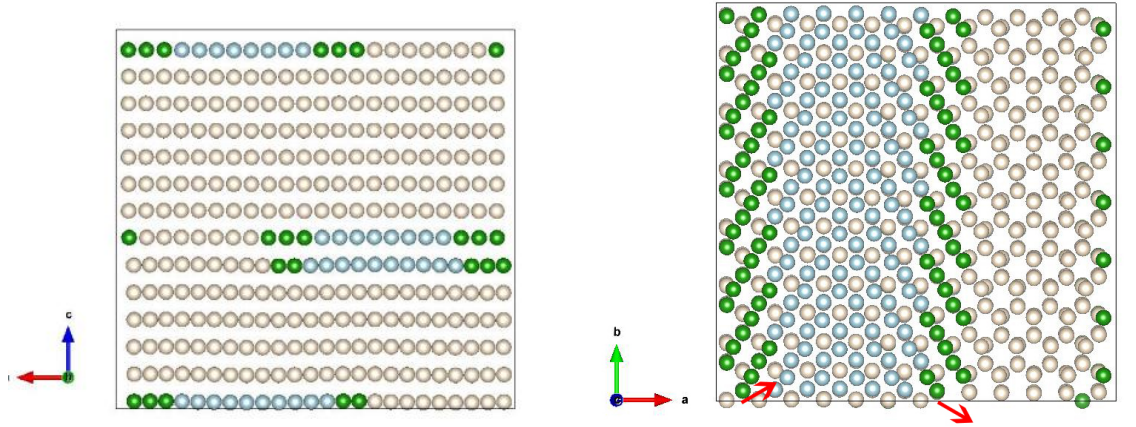


Figure 4.2: γ energy surface for a system of α -Zr. The global minimum are at the four corners, where the system is in its perfect configuration. A metastable fault is located at the local minimum and indicated by the arrows. The lengths units are a_0 .



(a) View of the dislocation after the minimization from $(10\bar{1}0)$. Notice the arrangement of the principal dislocation and the dislocation at the boundary in an oblique pattern to reduce the stresses at the dislocation cores.

(b) View of the dislocation after the minimization from (0001) . The arrows show the partial Burgers vector for each of the partial dislocations. Notice the sum of both vectors give the total Burgers vector introduced at the beginning.

Figure 4.3: Illustration of the resulting system after the minimization of the potential energy through a conjugate gradient algorithm. In the figure, we can distinguish three arrangement of the atoms according to their coordination number. The green ones belong to the dislocation core, the blue ones are the stacking fault and are arranged in a fcc lattice and the pastel ones have the common hcp coordination number

is the dislocation and what are the features of the partial dislocations. In Fig. 4.4 one can observe the distribution of the Burgers vector for a system of 18424 atoms. In this picture, we show four different plots with three different curves in each of them. The upper plots refer to the displacement of the atoms with respect to the perfect lattice, while the lower graphs depict the derivative of the above plots; thus they show the components of each of the Burgers vector (b_x, b_y) . Each of the different curves shows a way in which the relaxation has been performed. The blue line reproduces the data obtained from a relaxation where the box is relaxed and the potential is shifted, the green line does the same but without relaxing the box and the red line neither relaxes the box nor shifts the potential. Independently of the case, we see how the screw component is zero in modulus and the edge component is equal to a_0 , when integrating over the axis containing the initial Burgers vector, x . As observed, the most relevant feature of the relaxation is whether we relax the box or not, since the shift in the potential does not trigger a great difference. The separation between the partial dislocations is $\sim 10a_0$ for the green line, $\sim 9a_0$ for the red line and $\sim 12a_0$ for the blue line. Therefore, the relaxation of the box makes the partial dislocations move away from each other as most as possible. This is consistent with the fact that the original box is enlarged in the x direction to minimize the stresses during the box relaxation. Also, we observe how the partial dislocations in the similar cases are ordered $+30^\circ$ and -30° , whereas in the latter case are ordered the other way round, -30° and $+30^\circ$ with respect to the initial Burgers vector. In Fig. 4.3a we have indicated the partial Burgers vectors with a red arrow. The magnitude of the partial Burgers vectors is $b_p = b/\sqrt{3}$.

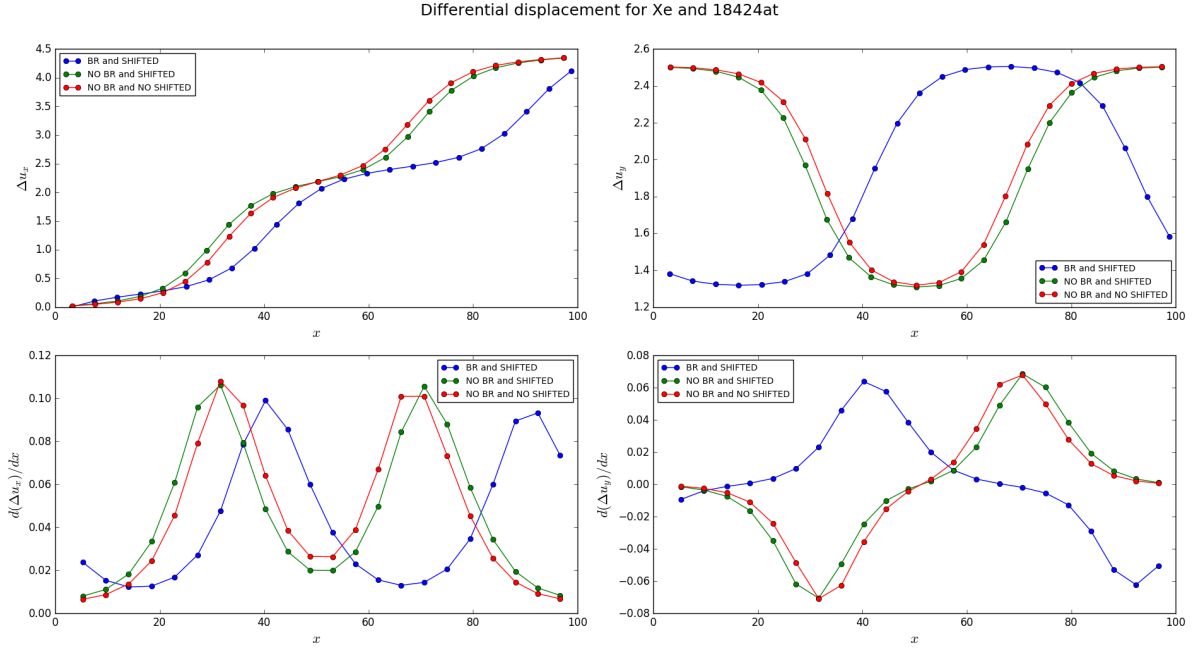


Figure 4.4: Plot of the relative displacement and the differential displacement of the atoms above and below the glide plane in the x and y directions. The curves of the plots represent a way in which the relaxation has been performed. The blue one represents the resulting system after a relaxation where the box has also evidence and the potential shifted, the red one when the box remains still and the potential shifted and the red one when the box is not relaxed broad and the potential is not shifted.

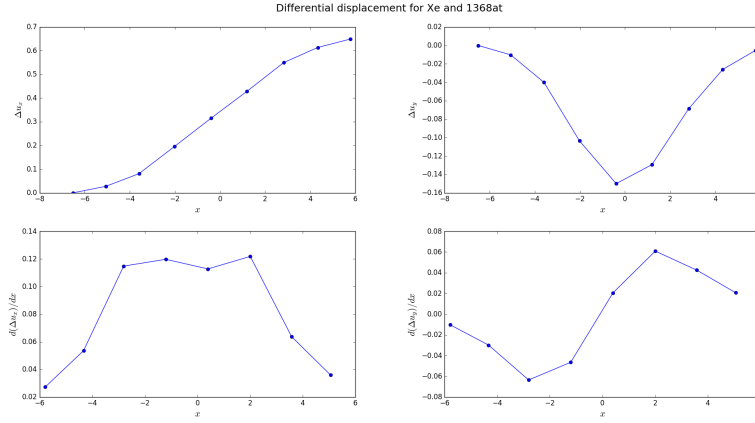
For the dynamic simulations, our initial configuration will be the resulting system after the relaxation with the shifted potential of both the system and the box. This is the case for which the energy and the forces are minimum

We have also performed a study of the effect of the system size on the relaxation of it. In Fig. 4.5 we can compare the resulting relaxed system for two different sizes. In Fig. 4.5a we represent the Differential displacement analysis for a system with $L_x = 10b$, whereas in Fig. 4.5b we plot the same analysis but for a much bigger system, with $L_x = 130a$. As shown in Fig. 4.5b, the partial dislocations tend to separate from each other as most as possible until they reach an equilibrium value of $\sim 210 \text{ \AA}$ ($\sim 50b$). The width of the peak in the equilibrium is $\sim 25a$, so the distortion introduced by the dislocation is significant. From the same plot, we can infer the width of the dislocation core, since it is defined as the region in which the disregistry is greater than the half of its maximum. Therefore, $d \approx 12.5a$. This constitutes a very wide dislocation core, consistently with the observation of a very mobile dislocation, as defined by Eq. 2.11

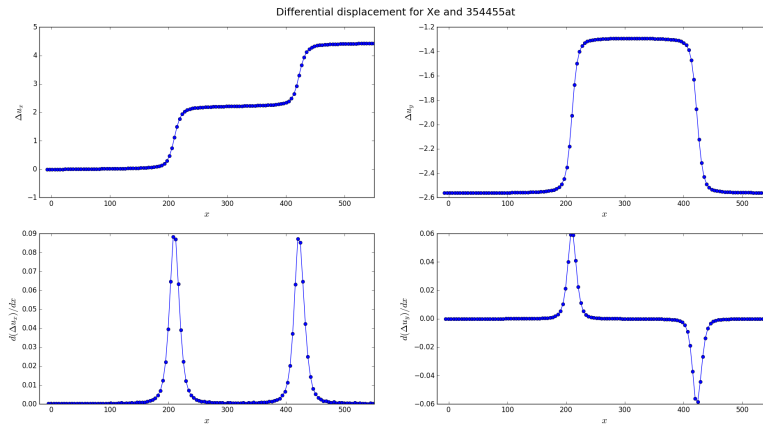
However, the value of the width of the stacking fault is far from the theoretical value predicted by the expression [22]

$$d = \frac{Gb^2}{4\pi\gamma_{SF}} \quad (4.1)$$

where $b = 4.26$ is the partial dislocation Burgers vector, G is the shear modulus and γ_{SF} is the stacking fault energy. Unfortunately, we have not been able to find these



(a) Atomic disregistry due to a dislocation in a system of 1368 atoms.



(b) Atomic disregistry due to a dislocation in a system of 344544 atoms.

Figure 4.5: Illustration of the disregistry of two system with different sizes. In both of them we have computed the displacement difference and the differential displacement to asses the positions and configurations of the partial dislocation cores and the stacking fault.

values in the literature. Nonetheless, we can take as a reference the predicted value of Borda *et al.* [19] of $d = 434 \text{ \AA}$ for the case of quantum ^4He , which is a rare gas as well and the type of interaction is not extremely different from the one of Xe.

The alignment of the dislocation in the boundary (half at the top and half at the bottom) and the principal dislocation in an oblique pattern is a direct consequence of the different image stresses that occur due to the periodic boundary conditions. This arrangement is in good agreement with the predicted by the anisotropic elasticity theory, for instance, see the Supplemental material of [19] for an analysis using this theory.

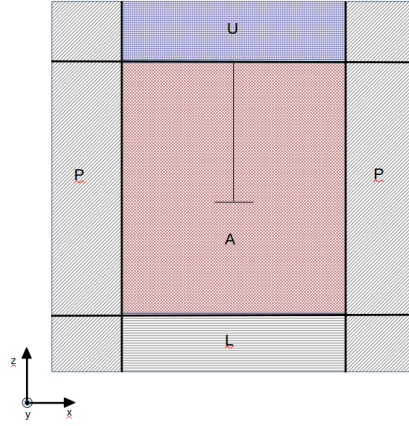


Figure 4.6: Schematic representation of the system employed to retrieve the Peierls stress in Method 1. We can differentiate three parts: U the upper part, L the lower part and A the region of mobile atoms. The letter P indicates the periodic images.

4.1.1.2 Peierls stress

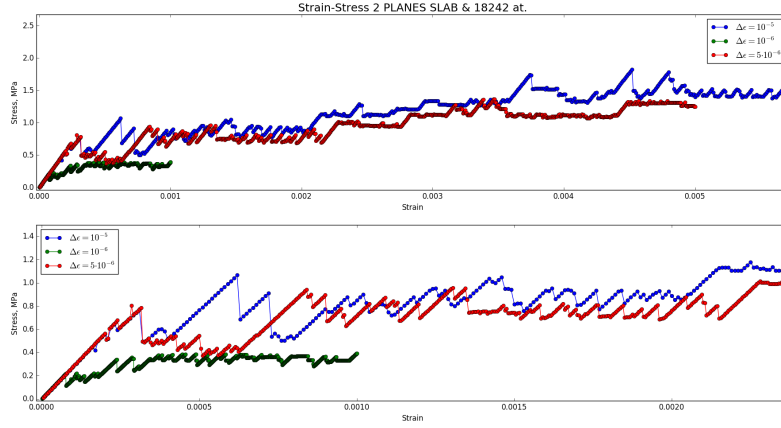
The Peierls stress is a key quantification of the lattice resistance to dislocation motion in a crystal. This value is commonly referred as the critical shear stress (CRSS) for glide at $T = 0K$. In the present work, we have used two methods to compute this value, which should retrieve similar results.

1st Method

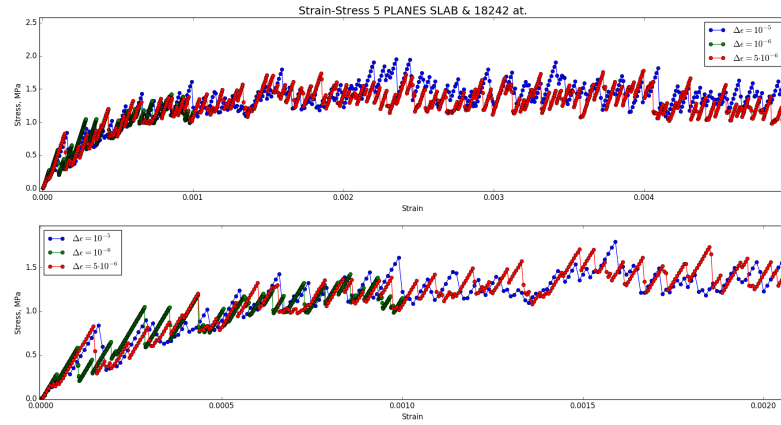
This procedure is the most reported one in the literature and it is the most used among researchers to compute the Peierls stress τ_p [24,47]. This method consists of dividing the solid into three different regions, U -the upper part-, A -the region of mobile atoms- and L -the lower part- along the z axis and displacing U a certain increment while relaxing the region of mobile atoms. Fig.4.6 shows an scheme of the division of the system. In our case, since the dislocation line is parallel to the y axis, we displace the upper slab of the crystal an increment Δu in the x axis. Hence, we can depict the $\epsilon_{xz} - \sigma_{xz}$ graph, where the strain ϵ_{xz} is $\epsilon_{xz} = \Delta u / L_z$ and the shear stress is $\sigma_{xz} = F_x / L_x L_z$, where F_x is the sum of the forces exerted on the atoms of the upper part. After each displacement, we minimize the potential energy until the A region of the system reaches the equilibrium. The atoms in the L and the U regions are freeze and fixed to their positions after the displacement.

The results obtained are found to be very sensitive to the size of the system and to the thickness of the upper region we pick. Also, it is important to choose a proper strain increment. In Fig. 4.7 we can appreciate the effects of the size of the upper region in the computation of the Peierls stress. For the narrower slab, we obtain much more inaccurate results and they are not consistent since for a slight increment of the strain we obtain substantial differences than for the others. The results correspond to a system of 18424 atoms, contained in a box of $L_x = 26b$ and $L_z = 12c$.

The stress profiles obtained from this simulations are not very satisfying. We would have expected to get a first part of the plot showing a linear profile, exhibiting the



(a) Evolution of the stress as a function of the strain in a crystal of 18424 atoms and where the upper slab is formed by a region of vertical size of $\sim 1c$



(b) Evolution of the stress as a function of the strain in a crystal of 18424 atoms and where the upper slab is formed by a region of vertical size of $\sim 2.5c$

Figure 4.7: The lower plots of both figures are a zoom in of the upper plot, in order to be able to observe the elastic behavior of the crystal.

elastic behavior of the crystal, until the dislocation is strained enough to move to the next valley of the energy surface, indicated by a sharp drop in the shear stress; and this repeated periodically. A hint of this behavior is shown in our simulations; however, it is not as regular as others have reported, for instance, see [47] or [24]. Although, we have made an estimation of the Peierls stress from Fig. 4.8. We have averaged the stress value since the point of the strain at which the dislocation starts to move, which consistently coincides with the maximum of the stress value obtained, until the end of the simulation. This estimation gives us a reference value of $\tau_p = 1.759 \pm .17116 MPa$

To prove the accuracy of the method, the Orowan formula gives a theoretical relationship between the plastic shear strain ϵ , the mean distance of the dislocation motion \bar{x}

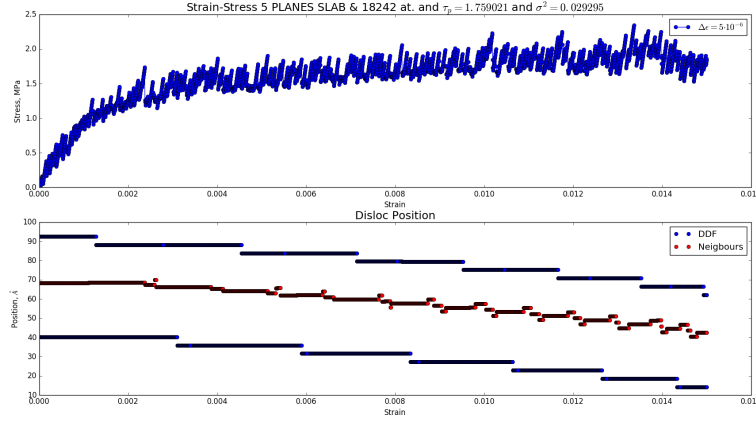


Figure 4.8: Evolution of the stress as a function of the strain in a crystal of 18424 atoms and the dislocation position as a function of the same strain.

and the dislocation density ρ_D [22]

$$\epsilon = \bar{x}b\rho_b = \bar{x}\frac{b}{L_x L_z} \quad (4.2)$$

which substituting the values obtained in our simulations, $\bar{x} = 6b$, we get

$$\epsilon = 0.01001 \quad (4.3)$$

In our simulation we have that at the point the dislocation starts to move $\epsilon_{ini} = 0.0031$ and the strain for which the dislocation has moved over 6 Burgers vector is $\epsilon_{6b} = 0.0143$. Therefore, the difference in the strain is $\Delta\epsilon = \epsilon_{6b} - \epsilon_{ini} = 0.0112$, which is in good agreement with the obtained value.

Osetsky and Bacon [47] report that accurate results for this analysis are only obtained when simulating a box with $L_x \geq 130b$ and $L_z \geq 80c$ (These are the lengths of the sides of the plane perpendicular to the dislocation line). Therefore, we have constructed a system of 354455 atoms and the mentioned box sizes to perform the same simulation. The results obtained are shown in Fig. 4.9. Notice the regular pattern obtained for the stress in Fig. 4.9. The Peierls stress obtained in this case is $\sigma_p = 0.6415 \text{ MPa}$. This value is far from the obtained with the system of 18424 at, meaning that the size effects are very significant, but it allows us to estimate the order of magnitude of the Peierls stress to be around $\sim 1 \text{ MPa}$. In the latter case, the displacement every step is larger, $\Delta u = b/10$.

It is important to stand out the boundary conditions used in this attempt to obtain the Peierls stress. In this case, we have used PBC in the glide plane directions, but non PBC in the $+z$ direction, since it will make another dislocation appear above and under the system. This is not a problem for the classical case, since the simulation of a system without PBC is within the range of our possibilities, however, for the quantum computations we strictly need the use of PBC to be able to get reliable results, since we are very limited on the size of the system. Moreover, in this method a part of the system, U and L, does not take part in the relaxation of the system since they are forced

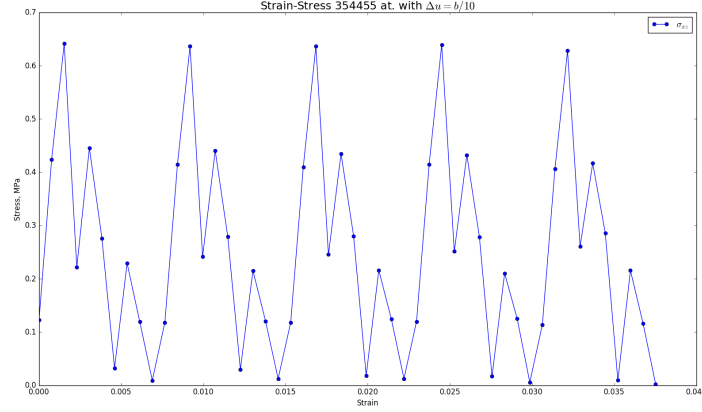


Figure 4.9: Evolution of the stress as a function of the strain in a crystal of 354455 atoms and the dislocation position as a function of the same strain.

to stand still. Once again, this procedure is unfeasible for the quantum simulations. This is the reason why we need to seek for an alternative way of computing the Peierls stress.

A possible way to solve the boundary problem is to introduce a system with a dipole of dislocations on it, or even better, with a quadrupole of dislocations, which allow us to apply boundary conditions and it reduces the effect of the image dislocations.

2nd Method

This second method attempts to reproduce the same results achieved by the other method by studying the energy of the system at every step. In other words, in this approach, we simply modify the box by adding a tilt (xz, xy, yz) , remapping the atoms according to this tilt and relaxing the system to reach its minimum in the potential energy surface. After the tilt, the box is not anymore orthogonal but triclinic. The lattice vectors that describe it are: $A = (a, 0, 0)$, $B = (xy, b, 0)$ and $C = (xz, yz, c)$. This deformation will introduce a shear stress into the system that can be computed by means of the derivative of the energy with respect to the strain. In the present case, we will only introduce a xz tilt. The exact expression is as follows:

$$\sigma_{xz} = \frac{1}{V} \frac{\partial E}{\partial n_{xz}} \quad (4.4)$$

where σ_{xz} is the shear stress (MPa) applied to the system by the deformation, E is the potential energy of the system, i.e. the potential energy since we are at $T = 0K$, and $n_{xz} = xz/L_z$ is the displacement strain defined from the tilt factor xz . In this method we use PBC in all three directions, to make a more realistic approach, despite the creation of other dislocations at the boundaries.

For the previous system of 18424 at. and 2240 at. we compute this analysis. In Fig. 4.10 we plot the energy of the system, the stress of the system and the position of the dislocation as a function of the strain for the system of 18424 atoms. For the smaller system, we obtain roughly a similar profile. The energy profile is consistent with the expectations since it shows a certain periodicity distorted by the presence of

a dislocation. From section 2.2.4 we know that the Peierls stress, τ_p , is defined as the maximum slope of the energy profile. Therefore, for these cases we obtain:

$$\tau_p^{18242at.} = 3.3756694 \text{ MPa}; \quad \tau_p^{2240at.} = 5.2336159 \text{ MPa} \quad (4.5)$$

These values are rather small and agree with the observed in method 1 and in the finite temperature simulations, where almost no lattice resistance opposes to the movement of the dislocations. However, an intriguing fact arising from the dislocation position plot makes us doubt on these results. Fundamentally, the Peierls stress is defined as the shear stress at which the dislocation starts to move at $T = 0K$. In the observed plots, the dislocation moves for values of the shear stress $\sim 1.1 \text{ MPa}$. This value is much smaller than the global maximum, but it "coincides" with the local maximum. Moreover, it is in better agreement with method 1, so we take this value as the Peierls stress obtained from method 2.

In Wang's *et al.* work [48], they fit the profile of the energy to a mathematical function related with the elasticity theory. In our case, although the profile of the energy exhibits a periodic curve, we have not been able to fit the data to a suitable function. Choicely, as explained, we have relied the observations on the fundamentals of the Peierls stress relating the shear stress values to the motion of the dislocation.

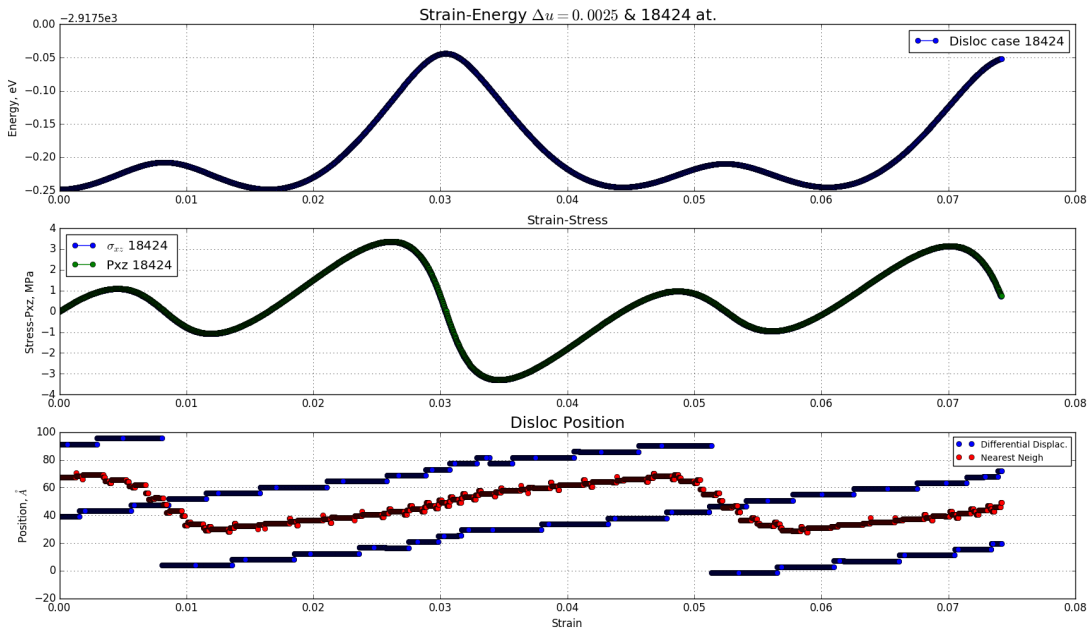


Figure 4.10: Representation of the Energy (eV), the shear stress σ_{xz} (MPa) and the position of the dislocation (Å) as a function of the strain for a system of 18424 atoms.

Analoguely to Method 1, we calculate, via the Orowan formula, if the theoretical expectations match the experimental results. In this case the mean dislocation motion $\bar{x} =$ and the box sizes are the same as before, $L_x = 26b$ and $L_z = 14c = 14 \cdot 1.633b$. Therefore,

$$\epsilon = \bar{x}b\rho_b = \bar{x} \frac{b}{L_x L_z} \quad (4.6)$$

where substituting the values obtained in our simulations we get

$$\epsilon = 0.02523 \quad (4.7)$$

In our plot, we obtain a strain of 0.0629 to move the mentioned distance, which is far from the theoretical value. The strain for which the dislocation starts to move does coincide with the strain observed in Method 1.

A possible inaccuracy that led us to wrong results might be the forces of the periodic images and the fact of having a dislocation at the boundary.

In this sense, to compute the size and the image force effects we have performed the same analysis for three different systems, the first one consisting of a system of 1368 atoms with a single dislocation, the second one is a quadrupole of dislocations, as shown in Fig. 4.11a, with 5472 atoms and a third much bigger one with 247680 atoms containing a quadrupole too. The introduction of a quadrupole is the unique way to vanish the periodic image forces in the dislocation cores. Nonetheless, after the first tilt

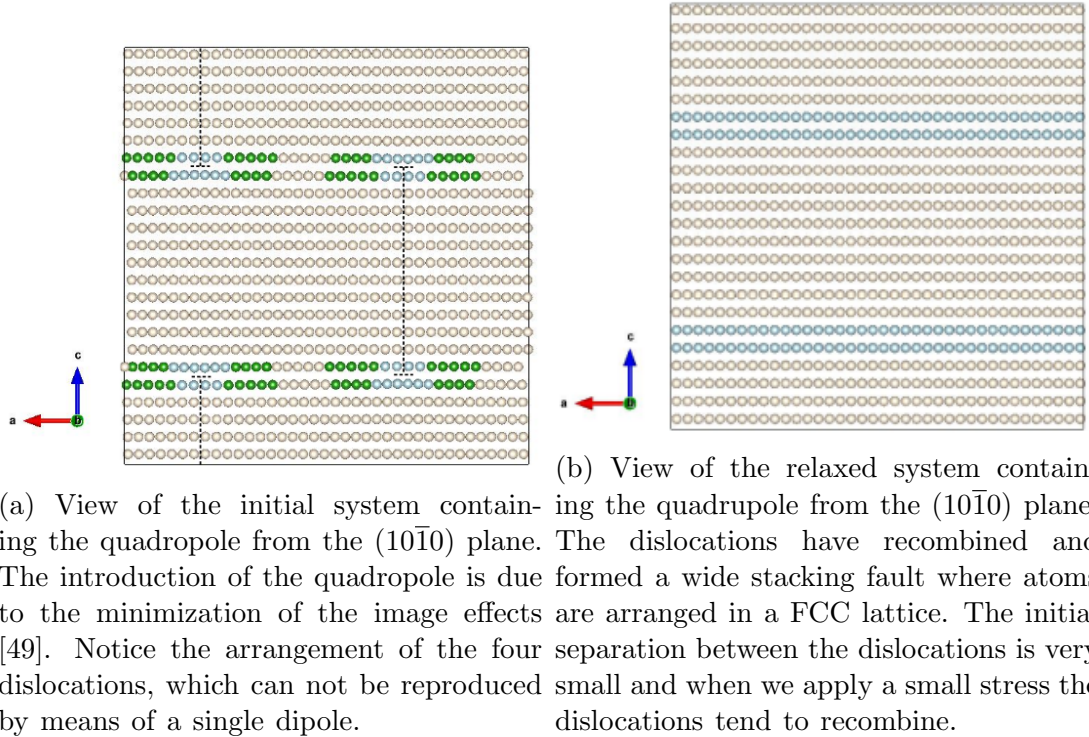


Figure 4.11: Quadrupole of dislocations in a box containing 5472 atoms and with $L_x = 20a$.

of the box, the dislocations seem to merge into one big stacking fault, recombining and disappearing, as shown in Fig. 4.11b. Obviously, this deceiving behavior disables us to compute the value of the Peierls stress. If we wanted to perform the computation this way, we would need a huge system, where the partial dislocations are too far from each other to interact.

In Fig. 4.12, we plot the Differential displacement analysis for the quadrupole case. We would have expected four peaks in the differential displacement in the x direction,

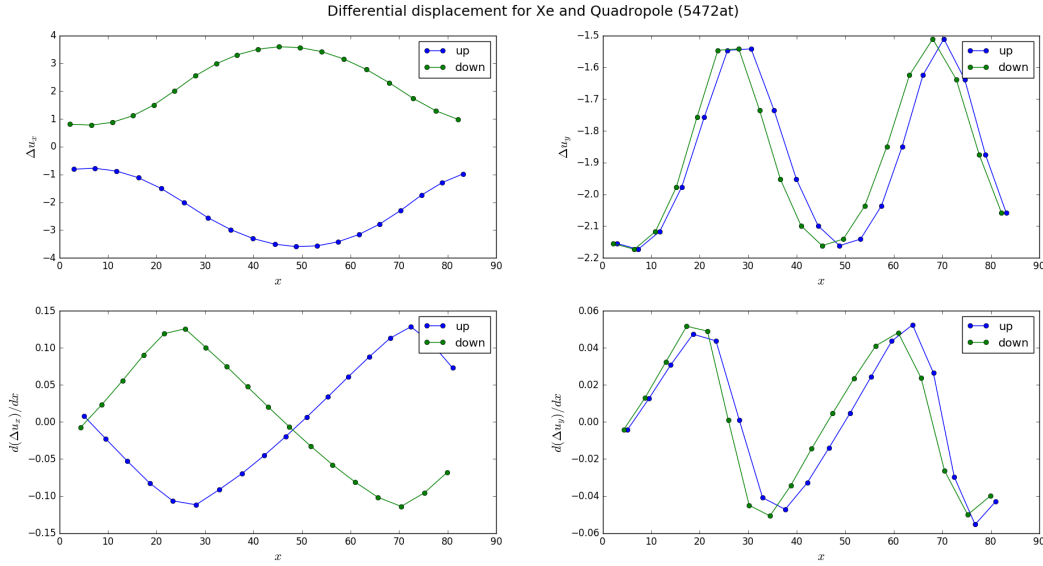


Figure 4.12: Plot of the relative displacement and differential displacement in the planes where the dislocations were introduced. The green curve depicts the DD and relative displacements of the planes of the dislocations of the upper part of the box, whereas the blue one describes the distortion of the atoms in the lower dislocation

since there are four partial dislocations, but only two appear. We assume this is due to the interaction between the dislocations, that somehow balance the displacement of the atoms. In the y direction we obtain the expected results, with four peaks and a value of zero for the screw component of the Burgers vectors (the integration is null).

To get an estimation of the size error it would have been interesting to perform the same simulations but introducing a dipole rather than a quadrupole. We know this scheme will be more sensitive to the image forces than the quadrupole, but less than a single dislocation. Once again, this has been imposible due to time constraints.

4.1.2 Finite temperature properties

In this section, we show the results obtained from the simulations of a system with a single dislocation at a finite temperature. The system is relaxed from the initial configuration, as introduced previously. The boundary conditions applied to the simulations are PBC in the glide plane axes, i.e x and y , and in the z direction. However, the simulation box is enlarged in the $+z$ and $-z$ edges to create a vacuum gap between the vertical images. This procedure is done to avoid the creation of a second dislocation in the upper and lower edges that would interact with the principal dislocation.

We have performed different simulations using different ensembles and different box sizes, $L_x = 12a$ (2240 atoms) and $L_x = 26a$ (18424 atoms). The temperatures at which we have carried out the simulations are rather low, $25K$ and $50K$. For the NVT and NPT ensembles, the temperature is fixed through the simulation and, in the case of the NPT, the pressure is set and fixed to zero as well. Also, the shear stresses are forced

to be zero in the latter case. In the NVE simulation, we set the initial velocities to be the corresponding ones to a kinetic energy of $25K$, by the equipartition theorem. Then, at the beginning of the simulation, half of this kinetic energy transforms in potential energy, since the total energy (E) of the system must be conserved in this ensemble. Therefore, the decrease in the kinetic energy provokes the temperature to drop to a half of its initial value, $12.5K$ and $25K$, respectively. The simulations are performed with a timestep of $\Delta t = 1 fs$ and 800000 steps long, resulting in simulations of $800ps$.

The results obtained for each simulation are exhibited in Figs.4.13, 4.14, 4.15 and 4.16.

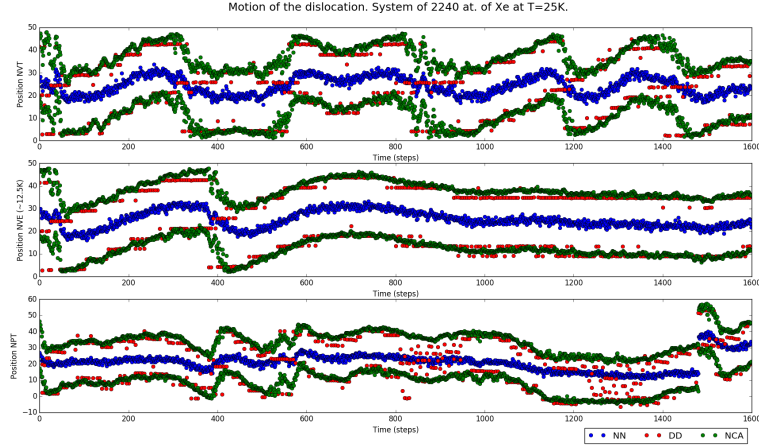


Figure 4.13: Representation of the position of the dislocation versus the time expressed in simulation time steps. The system is formed by 2240 atoms and the temperature of the system is fixed to 25 K through all the simulation. The simulation has been performed using three different ensembles, *NVT*, *NPT* and *NVE*. In the case of the *NVE* ensemble, the system reaches the equilibrium at a temperature of 12.5 K

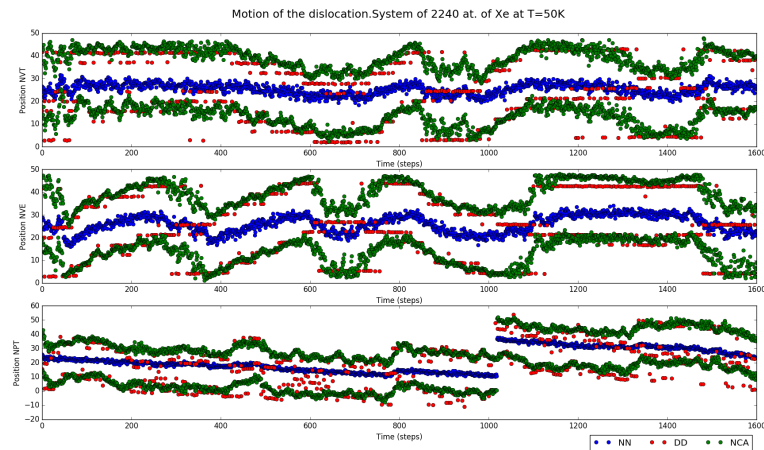


Figure 4.14: Representation of the position of the dislocation versus the time expressed in simulation time steps. The system is formed by 2240 atoms and the temperature of the system is fixed to 50 K through all the simulation. The simulation has been performed using three different ensembles, *NVT*, *NPT* and *NVE*. In the case of the *NVE* ensemble, the system reaches the equilibrium at a temperature of 25 K

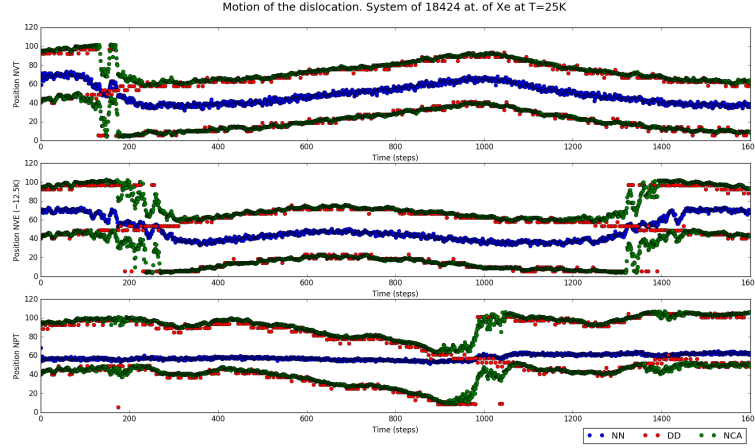


Figure 4.15: Representation of the position of the dislocation versus the time expressed in simulation time steps. The system is formed by 18424 atoms and the temperature of the system is fixed to 25 K through all the simulation. The simulation has been performed using three different ensembles, *NVT*, *NPT* and *NVE*. In the case of the *NVE* ensemble, the system reaches the equilibrium at a temperature of 12.5 K

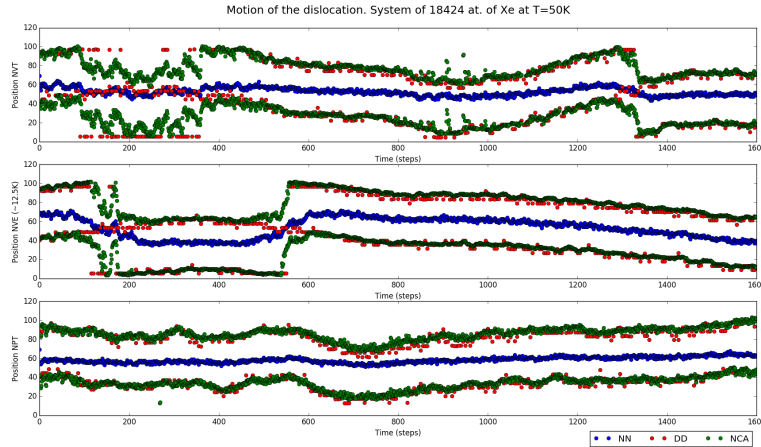
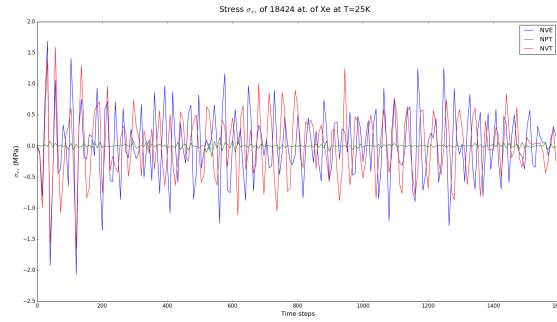


Figure 4.16: Representation of the position of the dislocation versus the time expressed in simulation time steps. The system is formed by 18424 atoms and the temperature of the system is fixed to 50 K through all the simulation. The simulation has been performed using three different ensembles, *NVT*, *NPT* and *NVE*. In the case of the *NVE* ensemble, the system reaches the equilibrium at a temperature of 25 K

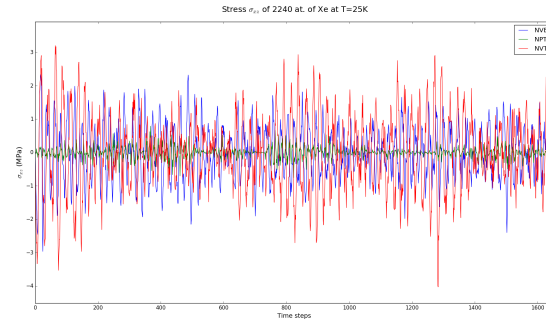
The position of the dislocation has been monitored with three different estimators to give consistency and robustness to the analysis. For the case of the differential displacement (3.3.3), due to its sensitiveness to the thermal fluctuations, we average the positions of the atoms over five timesteps, achieving very decent results. The other two methods of analysis are the study of the nearest neighbors (3.3.4) and the computation of the common neighbor analysis (3.3.5). The analysis of the nearest neighbors gives the blue curve in the plots, which is in the middle of the position of the partial dislocation cores. The reason for this is that, for the sake of simplicity, we have averaged the position of all the atoms that exhibited a different number of nearest

neighbors than twelve, obtaining the center of the stacking fault as a result. Due to the variation of the volume in the NPT simulation, the computation of the nearest neighbors gives erroneous results, so in these cases is better to look at the other two estimators.

Notice the movement of the dislocation when applying no shear stress at all. Cautiously, we regard the residual stresses that might affect the dislocation. In Fig. 4.17 we represent the temporal evolution of the σ_{xz} which is the candidate to be responsible for the movement of the dislocation. As observed, for the NVT and NVE ensembles it reaches values of 1.5MPa in Fig.4.17a and of almost 4MPa in Fig. 4.17b. Comparing these maximum values to the approximations of the Peierls stress obtained in section 3.1.1 it is consistent that there is movement under these residual stresses. Moreover, we want to emphasize the case of the NPT ensemble, where the stresses are very close to being null but we still observe some motion. This manifests the very low resistance of the lattice to dislocation movement since only with the energy coming from the thermal influence is sufficient to make the dislocation move.



(a) System of 18424 atoms



(b) System of 2240 atoms

Figure 4.17: Temporal evolution of the σ_{xz} component of the shear stress matrix at $T = 25\text{K}$

In addition, the stress values for the small (Fig. 4.17b) system are greater than in the big system (Fig. 4.17a). This is in good agreement with the fact that the periodic image forces are greater in the small box than for the bigger system.

The stacking fault bounded by the dislocations appear to attain an equilibrium width after a transient period. The mean values for each of the ensembles, box sizes and temperatures are shown in tables 4.1 and 4.2

25 K				
Ensemble/Size	2240 atoms		18424 atoms	
	Mean (Å (a))	Stand. Dev. (Å (a))	Mean (Å (a))	Stand. Dev. (Å (a))
NVT	26.5192 (6.0134)	1.792 (0.4064)	52.9240 (12.0009)	1.4029 (0.3181)
NVE	26.1663 (5.9334)	1.0816 (0.2452)	53.5605 (12.1452)	2.5636 (0.5813)
NPT	25.9512 (5.532)	2.0846 (0.4726)	53.2529 (12.0755)	2.5479 (0.5777)

Table 4.1: Widths of the stacking fault for the different sizes of the systems and ensembles at $T = 25K$. Notice that the value in parenthesis is expressed in lattice parameter units

50 K				
Ensemble/Size	2240 atoms		18424 atoms	
	Mean (Å (a))	Stand. Dev. (Å (a))	Mean (Å (a))	Stand. Dev. (Å (a))
NVT	26.2852 (5.9603)	2.1225 (0.4812)	52.6132 (11.9304)	14.7192 (3.3377)
NVE	26.6292 (6.0383)	1.7208 (0.3902)	52.5226 (11.9098)	14.6723 (3.3270)
NPT	26.0362 (5.9039)	2.4744 (0.5611)	52.5689 (11.9203)	14.7481 (3.3442)

Table 4.2: Widths of the stacking fault for the different sizes of the systems and ensembles at $T = 50K$. Notice that the value in parenthesis is expressed in lattice parameter units

The average distance between the two partial dislocations, or analogously, the width of the stacking fault region, does not vary with the temperature or the ensemble. Indeed, it is the same as the one observed after the relaxation. The standard deviation, although small, seems to be slightly bigger in the NPT case than for the other cases. Due to the thermal fluctuations being bigger at $T = 50K$ than at $T = 25K$, the standard deviation of both systems grows with the temperature as well. Once again, as indicated in the Relaxation part of section 4.1.1, the width of the stacking fault is as big as the box allows it to be. Eventually, this width would arrive at an equilibrium, but that point is far from our scope due to size restrictions in our simulations.

4.1.3 About the boundary conditions

To emphasize the importance of the boundary conditions in atomistic simulations, consider the Avogadro's number, $N_A = 6.022 \times 10^{23}$, which is the number of atoms in one mole. Roughly, the order of magnitude of atoms contained in a cubic centimeter is of this order. In a simulation, although the fast development in computational sciences, we can handle from 10^3 to 10^6 atoms. Therefore, the atoms of a simulation are influenced by a large number of interacting atoms ($\sim 10^{23}$) that can not be taken into account explicitly, unless we want a simulation to take several years.

The search of suitable boundary conditions that allow simulating a more realistic environment more efficiently is still present today. Periodical boundary conditions permit us to avoid all the surface effect since there are no surfaces explicitly. The choice of the boundary conditions can alter the nature of the problem substantially since it will affect what determined atoms perceive.

In our work, we have faced many challenges when dealing with the boundary conditions.

At the very beginning, we used periodic boundary conditions in all three axes to perform all the simulations, since this type of boundaries are the most realistic ones when simulating a crystal. However, we encountered a big problem: the appearance of a second dislocation with Burgers vector opposite to the already known one. For instance, observe Fig. 4.3a to visualize it. The atoms colored in green at the upper and lower boundary are a part of each of the dislocations in the boundary. To avoid this effect, we have two possibilities; firstly, we can introduce a dipole of dislocations instead of a single dislocation or, secondly, we can apply other boundary conditions rather than PBC.

Introducing a dipole instead of a single dislocation is within our reach for the classical case; however, for the quantum case we are very restricted by the size of the box to fit two dislocations. We would have to employ a much bigger system than the one used for the quantum simulations to do so. Consequently, the computational costs would be much greater.

The fact of having PBC also means we have a dislocation (or a dislocation dipole or quadrupole) in every periodic image cell. These dislocations interact with each other, exerting forces on each other, which can "pollute" our final results substantially.

The advantage of the introduction of a quadrupole arrangement is that the superposition of the elastic stress fields produces zero stress at the dislocation centers. These means, the dislocation does not notice any other shear stresses that the one introduced by us.

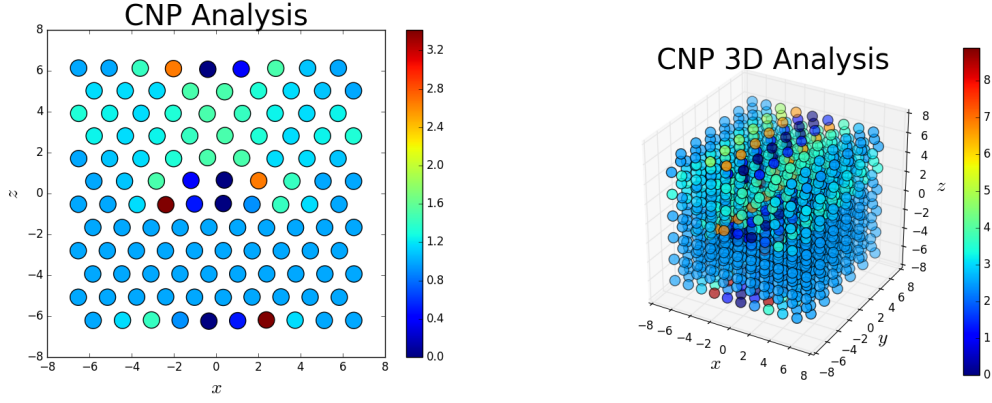
Consistently, these image-image interactions are reduced when enlarging the system, since the distance between dislocations is bigger. This procedure allows us to quantify the errors introduced by the images and validate whether the system is too small or not.

4.2 Quantum regime

The quantum simulations are based on a fully periodic cell containing a single dislocation. The initial configuration was created by the same method explained in the classical simulation, the extraction of a semiplane. It was relaxed to its minimum potential energy state by means of a conjugate gradient algorithm as done in the classical simulations.

As happened before, we face a problem when introducing a single dislocation and using PBC, since other two dislocations appear at the upper and lower boundaries. In this case, we are no longer capable of avoiding this problem due to the size restrictions we encounter. We have to conform ourselves with bearing it in mind when analyzing the results. Our system contains 1368 atoms, distributed in a box of $L_x = 13.7417\sigma$ ($10b$), $L_y = 14.2808\sigma$ ($6b$) and $L_z = 13.4640\sigma$ ($6c$), where $\sigma = 2.556\text{ \AA}$. Hence, the Burgers vector magnitude is $\sim 3.74\text{ \AA}$ and the density is $\rho = 0.5177\sigma^{-3}$. Fig. 4.18 show the 2D and 3D representations of the initial configuration of the system. The different colors show the structural arrangement of each atom. A color equivalent to zero means the atom is arranged in a fcc lattice, whereas a value between 2 and 3 means it is in a hcp region. Higher values of this parameter indicate an unknown

arrangement, so these are the atoms forming the dislocation core. Fig. 4.19 show the initial disregistry analysis of the relative displacement between the atoms above and below the slip plane. The figure displays a very narrow stacking fault region with almost no dissociation of the dislocation. The reason why this occurs is due to the small size of the simulation box; that does not allow the dislocation to dissociate due to periodic image forces.



(a) CNP analysis of an arbitrary $x - z$ plane.

(b) CNP analysis in 3D

Figure 4.18: CNP analysis of the initial configuration of the quantum simulation.

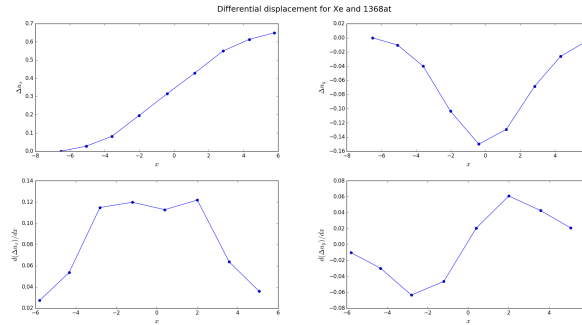


Figure 4.19: DD analysis of the initial configuration of the quantum simulations

The choice of making the system bigger in the $x - z$ plane, as done for the very big systems in the classical simulations, to reduce the periodic image forces was discarded since the reliability of the calculation of the superfluidity lies on the width of the box in the y direction. A very narrow box in the y direction could lead the system to show superfluidity wrongly [50,51].

Several simulations at different temperatures, i.e $3K$ and $1.5K$, were carried out. For each of these temperatures, we performed a simulation of 100 Monte Carlo steps and 100 steps per each block. The Chin approximation [38] is used to compute the thermal density matrix and the Worm algorithm [39–41] is used for the permutation sampling. The atoms interact through a pair action based on the Aziz potential [52].

We have been able to compute other properties for the system with the dislocation during the simulation. Fig. 4.20 shows the evolution of the energy and its fluctuations

T	σ_{kin} (%)	σ_{pot} (%)	σ_{tot} (%)
1.5 K	0.06707	0.00907	0.36434
3 K	0.901133	0.10054	4.61865

Table 4.3: Mean standard deviations (σ) of each of the components of the energy for a system of solid ^4He at $T = 1.5K$ and $T = 3K$.

around an equilibrium value for each of the two simulations performed. The mean standard deviation averaged over the last 25 steps are summoned in table 4.3. As observed, the standard deviations prove that the simulations have not yet converged to the equilibrium value. Conventionally, an admitted value for σ to consider the system has reached its equilibrium is of the order of $0.1\% - 0.01\%$. The results obtained indicate the simulations done are too short, particularly for the case of $T = 3K$, where the standard deviation is much greater than the admitted values. For the case of lower temperature, $T = 1.5K$, the system is very close to the equilibrium, but not there yet. This might be a reason why we have not been able to obtain meaningful results in the study of the dislocation movement, as explained afterward.

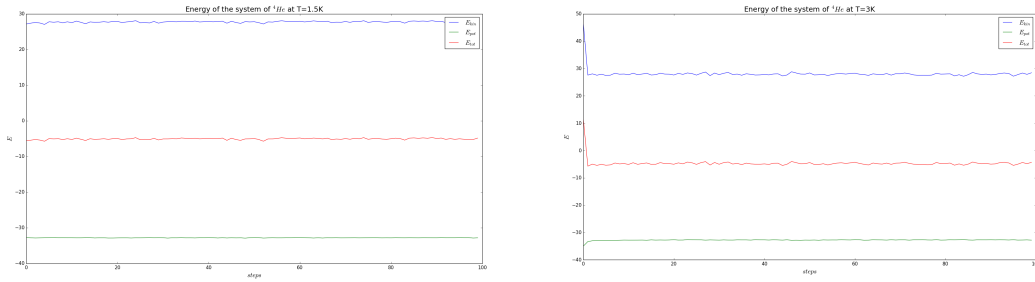


Figure 4.20: Energy of the system of solid ^4He at $T = 1.5K$ (a) and $T = 1.5K$ (b). The fluctuation of the total energy is for each system are exhibited in table 4.3

Some doubts about the solidity of the system arose from the structural configuration of the system at the temperature of $T = 3K$ which is very close to the melting point. Fig. 4.21 and Fig. 4.22 exhibit the radial distribution function (a) and the static structure factor $S(k)$ (b). The radial distribution function gives an idea of the distance between atoms. In the perfect static case the plot are Dirac deltas. On the other hand, the static structure factor shows the periodicity of the system. A high peak in the $S(k)$ means the system is very periodic and, therefore, the crystal structure is maintained. Although the peak for the $S(k)$ is not extremely high, for both temperatures we obtain a very similar structural configuration, ensuring that for $T = 3K$ it is still solid. The reason why the peak is not very well defined might be due to the distortion introduced by the dislocation, which breaks the periodicity of the lattice.

To analyze the outcome results we have tried both on-the-fly and *a posteriori* methods. In the first case, we computed the DD, Nearest neighbors and NCP analysis every 5 Monte Carlo timesteps. This way we avoided the need for storing an immense data file with the position of all the beads at certain timesteps. However, the inaccuracy of the results given by this method suggested to try *a posteriori* analysis. Also, the on-

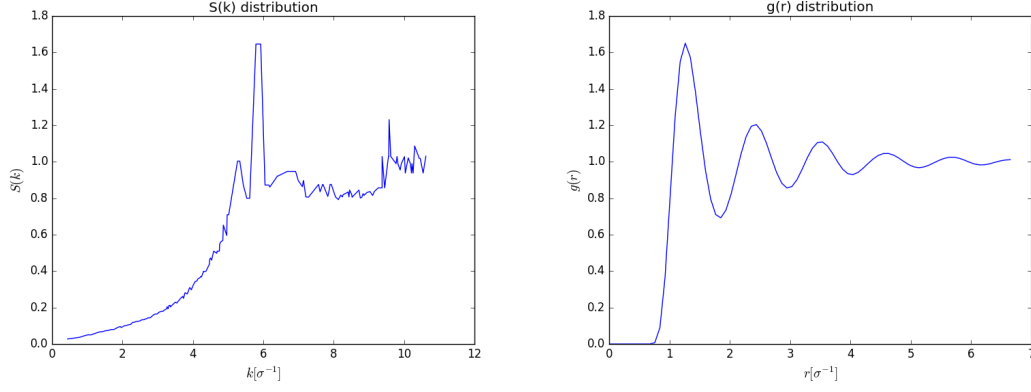


Figure 4.21: Radial distribution function (a) and static structure factor $S(k)$ (b) resulting from the simulation of ^4He at $T = 1.5K$.

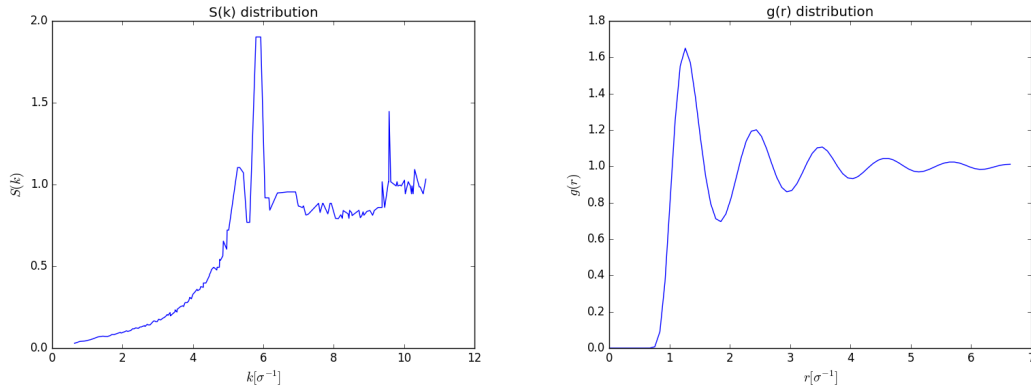


Figure 4.22: Radial distribution function (a) and static structure factor $S(k)$ (b) resulting from the simulation of ^4He at $T = 3K$.

the-fly method of analysis does not allow us to compute a calculation over an averaged value of the positions easily. Then, to perform *a posteriori* analysis, we computed the simulation saving the beads positions averaged over five timesteps. We found the zero-point motion of the atoms to be greater than expected and, therefore, we had to average their positions to get accurate values for the structural estimators implemented. We handled with an equivalent classical system of $1368 \times \text{beads}$ which in the case of $1.5K$, where we use polymers of 192 beads, goes up to 262656 atoms. However, even in this case, we have not been able to extract much information about the core structure and mobility of the dislocation. The structural distortion introduced by the great zero-point motion summed with the restrictions on the size of the box do not let us perform an accurate analysis of the dislocation. In addition, the length of the simulation prevented us of having enough statistical data to analyze.

Due to lack of time, we have not been able to perform a longer simulation that enabled us to make a detailed study of the system in the equilibrium. Hence, we have neither been able to make an exhaustive study on the existence of superfluidity in the

dislocation cores. As a first approach, though, the system does not show any sign of superfluidity response. This follows what Borda *et al.* concluded in [19], not observing superfluid cores in the dislocations. However, the non-appearance of superfluidity in the dislocation cores in the work of Borda *et al.* could possibly be a result of a technical misinterpretation. The calculation of the superfluidity without the use of the worm algorithm, as is the case, is very restricted to systems of a few particles (~ 100 atoms).

Chapter 5

Conclusions

In this thesis, we have performed atomistic simulations in the same system by using both classical and quantum approaches. We have dealt with an hcp lattice structure containing a dislocation -or in specific cases more than one-, which is a line defect that mediates the plastic behavior of materials. Firstly, we have studied the behavior of the dislocation at the classical regime, both at zero and at finite temperatures. To do so, we have made use of an already built code (LAMMPS) that has permitted us to focus more on the results rather than in the Molecular Dynamics code implementation. Applying several methods of relaxation, we have achieved the most stable, and thus the most likely, configuration of the system at zero temperature. From this state, we have applied and developed some techniques to study the plastic features of the solid containing the dislocation employing the study of the Peierls stress. Secondly, we have performed numerical simulations of a similar configuration in the quantum regime by means of a Path Integral Monte Carlo method (PIMC). We have been able to reproduce some of the results obtained by other researchers in very recent reports such as Borda *et al.* [19]. Due to time constraints, we have not been able to fully extend our simulation study to the regime of low temperatures, in which interesting phenomena involving dislocations are expected to occur. We leave this piece of research as future work (see Chapter 6).

Next on, we report the main conclusions obtained at each of the parts of the thesis

5.1 Classical regime

5.1.1 Relaxation

As a first contact with the dislocations, we have relaxed the system utilizing several techniques in order to obtain the most stable state, i.e. the state of minimum energy and forces, after the extraction of a semiplane to create the dislocation in the lattice. We have tested how the final system can be quite sensitive to some details in the relaxation procedure such as the shifting of the potential or the relaxation of the box to minimize the forces and stresses. At the relaxed state, we have recovered a well-

known structure for hcp lattices with a dislocation, the dissociation of the dislocation into two Shockley partial dislocations bounding a stacking fault. Consequently, the atoms in the stacking fault region show up to be arranged in a fcc lattice. These results have been possible by the development of an algorithm to study the disregistry of the atoms, what it is often known as the relative displacement. As explained, the derivative of this function gives the corresponding edge and screw components of the Burgers vector, in the present case, (b_x, b_y) . Therefore, we observe how the initial dislocation splits up into two partial dislocations as follows:

$$\frac{1}{3}[11\bar{2}0] \rightarrow \frac{1}{3}[10\bar{1}0] + \frac{1}{3}[01\bar{1}0] \quad (5.1)$$

where $\frac{1}{3}[11\bar{2}0]$ is the initial Burgers vector of an edge dislocation with no screw component, and it splits up into two dislocations with individual non-zero screw component. The width of the stacking fault, which depends on the elastic properties of the crystal, has shown up to be very broad. Its theoretical width is out of our scope and, thus, we have observed that every time we enlarged the size of the box that contained the Burgers vector (in our case, L_x) we achieved a different, greater, width for the stacking fault region.

5.1.2 Peierls stress

We have implemented two different techniques to retrieve the value of the Peierls stress for the classical system of Xe. We have observed that comparing both methods we have not been able to achieve a final estimation of the Peierls stress, but we are capable of giving a guess in the order of magnitude of it, which seems to be enough to explain some of the results obtained at finite temperature. A consistent order of magnitude with the simulations would be $\tau_p \sim 1MPa$. This value is rather low and it is the cause of the motion of dislocations at finite temperature in the absence of external forces, only due to the thermal fluctuations. The computation of the shear stress by means of the first method developed is very sensitive to the box size and the upper slab size. In our simulations, it has shown up to give a very irregular pattern for the small boxes, when we expected a regular periodical profile as reported in many cases, for instance, see [24]. This is not a problem for classical simulations, since we have computational resources to overcome these difficulties, and, therefore, this method can provide a good estimation for the Peierls stress, as shown in Fig. 4.9 for the system of 300000 atoms. Nonetheless, for the quantum simulations, due to its intrinsic complexity, it seems unfeasible to perform simulations of more than a few thousand of atoms.

On the other hand, we have developed a method to compute the Peierls stress that, from a qualitative point of view, offers better results than the former one. In this approach, we recover a very smooth profile for the energy when tilting the box more and more. We certainly believe this method, when studied the errors induced by the size effects, is the most suitable to study the Peierls stress at zero temperature in the quantum regime.

5.1.3 Finite temperature

In chapter 4.1.2, we have simulated the previously relaxed system of Xe at certain finite temperatures, $T = 25K$ and $T = 50K$, with no stresses or external forces applied. We had the purpose of simply confirming our expectations of observing no motion at all. However, we observe movement of the dislocation under no stresses, other than the residual ones, manifesting the absence of almost any intrinsic lattice resistance for the system. We have distinguished two sources for this motion, depending on the ensemble used for the simulation. In the NVT and NVE ensembles, we have observed that a large residual stress, of the same order of magnitude of the Peierls stress τ_p , fluctuates in time, causing the dislocation to fluctuate as well. In the other hand, in the NPT ensemble, where we force the stresses to be as close to zero as possible, we conclude the motion is due to thermal fluctuations, which led the dislocation to move to one side or the other alternatively. This is an important conclusion since gives an evidence that the absence of lattice resistance to dislocation motion is not an exclusive feature of quantum systems, but it has more to do with the kind of interaction, i.e. the strength of the interatomic potential, between particles. Moreover, we observe the width of the dislocation remains constant throughout the simulation and its value coincides with the initial width, obtained from the relaxation.

5.2 Quantum regime

Motivated by recent experiments done in the field, we have computed the behavior of a single dislocation in a ^4He solid at very low temperatures, i.e $T = 1.5K$ and $T = 3K$. Although not being able to study thoroughly the dislocation itself, we have been able to compute the properties of the system with a dislocation. We have observed no sign of superfluidity, either in the cores of the dislocation, as reported by Boninsegni *et al.* [11], or the stacking fault region. Although, a possible cause why we have not observed either of those might be the high temperature at which we performed the simulations or their small length. In Boninsegni's *et al.* work, they span a temperature range from 0.2 to 1K, whereas, in Borda's *et al.*, they simulate the system at a temperature of $T = 0.267K$. These values are far from ours, 1.5K and 3K. Due to many doubts regarding the structural analysis of the system at $T = 3K$, we questioned if the solid had melted into a crystal or not. From the analysis of the radial distribution functions and the static structure factor, we concluded that it was still a solid for that temperature. These issues prevented us from doing a much longer simulation that could give us reliable and meaningful results.

The results provided by the on-the-fly estimators have shown up to be non-sense. Therefore, we have concluded that to develop a proper analysis of the dislocation motion and to be able to track the dislocation throughout the simulation, we have to average the positions of the beads over several time steps to reduce the zero-point motion effect.

Chapter 6

Further work

Throughout the thesis we have been able to cover most of the objectives proposed related to the classical regime, however, due to the appearance of unexpected results in this first part, we have not been able to perform an exhaustive analysis in the quantum regime. Therefore, in this section, we present the aspects that require further work and a path to follow in order to achieve the objectives we proposed at the beginning.

Concerning the quantum simulations, we have been able to make an approach to the simulation of a single dislocation in a solid of ^4He at low temperatures. Our first objective was to make a study of the behavior of the dislocation under quantum effects and to clarify the controversy of the supersolidity; however, many improvements must be done to extract conclusions from our simulations. Firstly, we should be able to reimplement the estimators in the PIMC code in order to make them work every some iterations after we have averaged the beads positions. The zero-point motion of the particles distorts the structure of the crystal, disabling us to compute the properties of the dislocation. Secondly, we should review the simulation of a single dislocation with PBC. It would be logical, if possible, to better simulate a dipole of dislocations to avoid problems at the boundaries. With these improvements and performing a larger simulation, we would be able, in principle, to achieve the same results as Borda *et al.* concerning the dislocation behavior, but better results upon the superfluidity of the stacking fault and the dislocation cores. In our PIMC code, it has been implemented the Worm algorithm that allows us to properly calculate the superfluidity for systems greater than a few hundreds of atoms. In Borda *et al.*, they do not make use of this algorithm (at least they do not mention it), so that is why we doubt in some of the technical aspects of their procedure and we think we could make a better study, at least concerning the quantum aspects of the simulation. Moreover, it would be interesting to span a greater range of temperatures, trying to go under a few dK. Bear in mind as a useful reference that the giant plasticity phenomenon has been reported to appear at $T \simeq 0.15K$, so it would be interesting to be able to achieve this temperature to contrast the experiments with the simulations.

Moreover, it would be important to perform a quantum static analysis of the system with a dislocation. This is, to calculate the properties at $T = 0K$. The *Path Integral Ground State* method allows us to perform such analysis, that would be very useful to assess the Peierls stress for the quantum system and to depict the stacking fault energy

surface γ as well. The study of both properties would give us an idea of the lattice resistance to motion of dislocation, and, therefore, the resistance to plastic deformation and the stability of the dissociation of the edge dislocation into two Shockley partial dislocations. In the end, we would be able to give a proper theoretical explanation to the facts observed in the experiments, such as Giant Plasticity, from a fundamental point of view.

Bibliography

- [1] A. F. Andreev and I. M. Lifshitz. *Sov. Phys. JETP* , 29 , 1107, 1969.
- [2] G. V. Chester. *Phys. Rev. A* 2, 256–258, 1970.
- [3] E.L Andronikashvili. *Zh. Eksp. Teor. Fiz.* 16, 780, 1946.
- [4] E. Kim and M.H.W. Chan. *Nature* 427, 225, 2004.
- [5] A. Leggett. *Physica Fennica*, 8, 125, 1973.
- [6] J.Day and J. Beamish. *Nature* 450, 853, 2007.
- [7] J. Reppy. Condensed matter: The supersolid’s nemesis. E. S. Reich, *Nature* 468, 748 (2010).
- [8] J. Reppy. *Phys. Rev. Lett.* 104, 255301, 2010.
- [9] D.Y. Kim and M. H. W. Chan. *Phys. Rev. Lett.* 109, 155301, 2012.
- [10] A. Haziot, X. Rojas, A. D. Fefferman, and J.R. Beamish and S.Balibar. *Phys. Rev. Lett.* 110, 035301, 2013.
- [11] M. Boninsegni, A. B. Kuklov, L. Pollet, N. V. Prokof’ev, B. V. Svistunov, and M. Troyer. *Phys. Rev. Lett.* 99, 035301, 2007.
- [12] A.B. Kuklov. *Phys. Rev. B* 92, 134504, 2015.
- [13] A.B. Kuklov, L. Pollet, N.V. Prokof’ev, and B. V. Svistunov. *Phys. Rev. B* 90, 184508, 2014.
- [14] M.W Ray and R.B. Hallock. *Phys. Rev. Lett.* 100, 235301, 2008.
- [15] M.W Ray and R.B. Hallock. *Phys. Rev. B* 79, 224302, 2009.
- [16] M.W Ray and R.B. Hallock. *Phys. Rev. B* 84, 144512, 2011.
- [17] M. W. Vekhov, W. Mullin, and R.B. Hallock. *Phys. Rev. Lett.* 113, 035302, 2014.
- [18] M. W. Vekhov and R.B. Hallock. *Phys. Rev. B* 90, 134511, 2014.
- [19] E. Borda, W. Cai, and M. de Koning. *Phys. Rev. Lett.* 117, 045301, 2016.
- [20] A Serra, D.J Bacon, and R.C Pond. *Acta Metallurgica* 36, Pag. 3183-3203, 1988.
- [21] V. V. Bulatov and W. Cai. *Computer simulations of dislocations*. Oxford University Press, Oxford, (2006), 2006.

- [22] D.Hull and D.J Bacon. *Introduction to Dislocations*. BH, 2011.
- [23] D.J. Bacon and M. H. Liang. *Philosophical Magazine A*, 53:2, 163-179, 1986.
- [24] H.A. Khater and D.J. Bacon. *Acta Materialia*, 2978-2987, 2010.
- [25] A Berghezan, A Fourdeux, and S Amelinckx. *Acta Metallurgica*, 9, 464, 1961.
- [26] R. Pessoa, S. A. Vitiello, and M. de Koning. *Phys. Rev. Lett.* 104, 085301, 2014.
- [27] E. Polak and G. Ribière. *Revue Francaise d'Informatique et de Recherche Opérationnelle*, 16, 35-43., 1969.
- [28] W. Cai, Li J., and Yip S. *Comprehensive Nuclear Materials*, pages 249-265, 2012.
- [29] D.J. Bacon and J.W. Martin. *Philosophical Magazine A*, 43:4, 883-900, 1981.
- [30] Murray S. Daw and M. I. Baskes. *Phys. Rev. B* 29, 6443, 1984.
- [31] Riccardo Rota. *Path Integral Monte Carlo and Bose-Einstein condensation in quantum fluids and solids*. PhD thesis, Universitat Politècnica de Catalunya, 2011.
- [32] Bernard Bernu and David M. Ceperley. Path integral monte carlo. In J. Grotendorst, D. Marx, and A. Muramatsu, editors, *Quantum Simulation of Complex Many-Body Systems: From Theory to Algorithms*, pages 51-61. John von Neumann Institute for Computing, 2002.
- [33] N. Metropolis, A. W. Rosenbluth, M. N. Rosenbluth, A. H. Teller, and E. Teller. *J. Chem. Phys* , 21 , 1087, 1953.
- [34] H. Trotter. *Proc. Am. Math.* , 10 , 545, 1959.
- [35] D. Ceperley. *Rev. Mod. Phys.* 67, 280, 1995.
- [36] M. Takahashi and M. Imada. *J. Phys. Soc. Jpn.* , 53 , 963, 1984.
- [37] M. Takahashi and M. Imada. *J. Phys. Soc. Jpn.* , 53 , 3765, 1984.
- [38] S. A. Chin and C. R. Chen. *J. Chem. Phys* , 117 , 1409, 2002.
- [39] N. V. Prokof'ev, B. V. Svistunov, and I. S. Tupitsyn. *Physics Letters A*, 238, 253, 1998.
- [40] M. Boninsegni, N. V. Prokof 'ev, and B. V. Svistunov. *Phys. Rev. E* , 74 , 036701, 2006.
- [41] M. Boninsegni, N. Prokof 'ev, and B. Svistunov. *Phys. Rev. Lett.* , 96 ,070601, 2006.
- [42] A. Stukowski. *Modelling Simul. Mater. Sci. Eng.* 20, 4, 2012.
- [43] Honeycutt and Andersen. *J. Phys.* 91 (19), pp 4950-4963, 1987.
- [44] H. Tsuzuki, P.S. Branicio, and J. P. Rino. *Comp. phys. Comm.* 177, 518-523, 2007.
- [45] S. Plimpton. Fast parallel algorithms for short-range molecular dynamics. *J Comp Phys*, 117, 1-19, 1995. <http://lammmps.sandia.gov>.
- [46] K. Momma and F. Izumi. *J. Appl. Crystallogr.*, 44, 1272-1276, 2011.

- [47] Yu N. Osetsky and D. J. Bacon. *Modelling Simul. Mater. Sci. Eng.* 11, 427-446, 2003.
- [48] G. Wang, Alejandro Strachan, T. Çagin, and W. A. Goddard. *Modelling Simul. Mater. Sci. Eng.* 12, S371-S389, 2004.
- [49] S. K. Yadav, R. Ramprasad, A. Misra, and X. Liu. *Acta Materialia* 74, pag. 268-277, 2014.
- [50] C. Cazorla and J. Boronat. *Phys. Rev. B* 88, 224501, 2013.
- [51] M. C. Gordillo and D. M. Ceperley. *Phys. Rev. Lett.* 79, 3010, 1997.
- [52] R. A. Aziz, F. R. McCourt, and C. C. Wong. *Mol. Phys.* , 61 , 1487, 1987.